6-7-2016

The Design and Testing of a Novel Batch Photocatalytic Reactor and Photocatalyst

Shawn Sasser
University of South Florida, shawnsasser@mail.usf.edu

The Design and Testing of a Novel Batch Photocatalytic Reactor and Photocatalyst

by

Shawn M. Sasser

A thesis submitted in partial fulfillment
of the requirements for the degree of
Master of Science in Chemical Engineering
Department of Chemical and Biomedical Engineering
College of Engineering
University of South Florida

Co-Major Professor: Venkat Bhethanabotla, Ph.D.
Co-Major Professor: John Kuhn, Ph.D.
Scott Campbell, Ph.D.

Date of Approval:
May 24, 2016

Keywords: Photocatalysis, Renewable Energy, Reactor Design, Upconversion

DEDICATION

The work involved in this thesis is dedicated to my mother and father, and my fiancé. My mother has always encouraged me to follow my dreams and achieve my goals. Without her encouragement, I may have never chosen to pursue chemical engineering as a career. My father has given me the strength to push through the difficult times through my education. His insightful advice has been reassuring to say the least. My fiancé's determination and work ethic inspired me to become a better student by doing whatever is necessary to achieve my goals. As a fellow chemical engineer, she was able to give me relevant feedback on my work throughout my master's degree program.

ACKNOWLEDGMENTS

First, I would like to acknowledge my co-advisors *Dr. Venkat Bhethanabotla* and *Dr. John Kuhn* for their guidance and support during my time as a graduate student. My committee member, *Dr. Scott Campbell*, provided insightful feedback during the designing stages of my work. Thank you *Dr. Campbell*.

I would like to acknowledge *Mr. Anthony Villicana* from the USF Engineering machine shop, *Mr. Ryan Armes* from Polaris Electrical Connectors, and *Mr. James Christopher* from the USF Physics machine shop for their high-quality machining skills. *Anthony* was able to machine the finely threaded light mount and the extra narrow o-ring groove with no problems. *Ryan* kindly took the time to machine the reactor cell, the heating element body, and the window trap flange in the R&D department of his company. After making some modifications to the diameter of the pipe-weld connectors, *James* managed to fit the connectors in the reactor cell ports produce near-perfect welds.

I would also like to Acknowledge *Mrs. Annie Meier* for kindly taking SEM pictures and EDS data of my samples at NASA's Kennedy Space Center and allowing me to shadow her during the process. Lastly, I would like to acknowledge my lab partners: *Jon Pickering, Debtanu Maiti, Andrew Orbeck, Daniel Russel, Jonathan Samuelson, Divya Suresh, Daniela Allbright, Kassie Ngo, Ryan Kent,* and *Yolanda Daza*. They provided friendship, advice, and encouragement during my experiences in the lab.

TABLE OF CONTENTS

LIST OF TABLES iii

LIST OF FIGURES iv

ABSTRACT vi

CHAPTER 1: INTRODUCTION 1
1.1 The Human Footprint on the Global Environment 1
1.2 Photocatalysis and its Applications 2

CHAPTER 2: MATERIALS AND CHARACTERIZATION 4
2.1 Introduction 4
2.2 Layered Double Hydroxides 4
2.2.1 Synthesis of Zn/Ga/CO_3-LDH 5
2.3 ZnO/GaN Solid Solutions 5
2.3.1 Doping with Rare-Earth Metal Ions 8
2.4 Synthesis of ZnO/GaN Solid Solutions 9
2.5 Characterization 9
2.5.1 Powder X-ray Diffraction 9
2.5.2 Diffuse Reflectance Spectroscopy 10
2.5.2.1 MATLAB Bandgap GUI 10
2.5.3 BET Surface Area 10
2.5.4 Scanning Electron Microscopy 11

CHAPTER 3: PHOTOREACTOR DESIGN 12
3.1 Motivation 12
3.2 Reactor Cell 13
3.3 Catalyst Bed 14
3.4 Irradiation Source 15
3.4.1 Interchangeable Mounted LED 16
3.4.2 Threaded LED Mount 17
3.5 Gas Delivery System 17
3.5.1 Bubbler 18
3.5.2 Bubbler Bypass 18
3.6 Recirculating Flow 18
3.6.1 Metal Bellow Compressor 20
3.6.2 Recirculation Loop 21
3.7 Integrated Heating Element 22
3.7.1 Resistance Heating Wire 22

3.7.2 Heating Element Body 22
3.7.3 Heating Element Temperature Controller 23
3.8 Hermeticity 23
3.8.1 O-Ring Assembly 24
3.8.2 Inlet and Outlet Connectors 25

CHAPTER 4: PHOTOCATALYTIC EXPERIMENTS 26
4.1 Design of Experiments 26
4.2 Startup Procedures 27
4.2.1 Cleaning 27
4.2.2 Sample Preparation 28
4.2.3 Purging the Reactor 29
4.2.4 Introducing Nitrogen and Water Vapor 29
4.2.5 Charging CO_2 30
4.3 Photocatalytic Reaction Procedures 31
4.4 Shutdown Procedures 31

CHAPTER 5: RESULTS AND DISCUSSION 32
5.1 Powder X-Ray Diffraction 32
5.2 Diffuse Reflectance Spectroscopy 35
5.3 BET Surface Area 37
5.4 Scanning Electron Microscopy 38
5.5 Energy Dispersive X-Ray Spectroscopy 39
5.6 Photocatalytic Experiments 41

CHAPTER 6: CONCLUSIONS AND FUTURE WORK 47
6.1 Conclusions 47
6.2 Future Work 49
6.2.1 Reactor Modifications 50
6.2.2 Band Edge Measurements of ZnO/GaN 50
6.2.3 Upconversion Photoluminescence of Er-Doped ZnO/GaN 50
6.2.4 Optimizing Performance of ZnO/GaN Materials 51

REFERENCES 52

APPENDICES 57
Appendix A: MATLAB Programs 58
A.1 Bandgap GUI 58
A.2 XRD Analysis Program 61
Appendix B: Instrumentation 67
B.1 Gas Chromatograph 67
B.1.1 Column 67
B.1.2 Detector 68
Appendix C: Supplementary Data 71

LIST OF TABLES

Table 2.1 Comparison of rates of photocatalytic reduction of CO_2. 7

Table 2.2 Mass of $Er(NO_3)_3 \cdot 5H_2O$ in LDH samples. 9

Table 4.1 Experimental design matrix with values of process variables and constants. 27

Table 5.1 Calculated crystallite sizes for the pure and Er-doped LDH and ZG samples. 34

Table 5.2 Calculated bandgaps for the pure and Er-doped ZG samples. 36

Table 5.3 EDS data for the LDH, ZG, and ZG-.025Er samples. 40

Table 5.4 Control experiment parameters. 43

Table C.1 Specifications for Thorlabs M405L2 LED. 72

Table C.2 Actual reaction parameters for photocatalytic and control experiments. 72

LIST OF FIGURES

Figure 3.1 Photoreactor P&ID and exploded drawing.....13

Figure 3.2 Diagram showing how the window-bed distance was determined. 14

Figure 3.3 Flow-pressure chart for fritted glass filters of various standard porosity ratings.....15

Figure 3.4 Spectrum of Thorlabs M405L2 LED. 16

Figure 3.5 Threaded mount for interchangeable LED. 17

Figure 3.6 Flow-pressure chart for MB-21 metal bellow compressor.....20

Figure 3.7 MB-21 metal bellow compressor. 21

Figure 3.8 CAD drawings of heating element body. 23

Figure 3.9 Exploded view of a cross-section of the reactor cell.....24

Figure 3.10 Images of welded pipe weld connectors for (a) the reactor inlet and outlet, and (b) thermocouple. 25

Figure 4.1 Image of a ZG sample loaded in the photoreactor cell.....28

Figure 5.1 XRD data for (a) all LDH samples and (b) LDH with and without stirring. 33

Figure 5.2 XRD data for the nitrided ZG samples.....33

Figure 5.3 Tauc plot for the pure ZG sample.....36

Figure 5.4 Zoomed in reflectance spectra for samples ZG-.10Er and ZG-.05Er.....37

Figure 5.5 N_2 Physisorption results for samples ZG and ZG-.025Er. 38

Figure 5.6 SEM images revealing the morphology of (a) ZG, (b) ZG-.025Er, (c) ZG-.05Er, and (d) ZG-.10Er 39

Figure 5.7 EDS spectrum for the ZG sample.....40

Figure 5.8 Chromatogram for the experiment with TiO_2. 41

Figure 5.9 Chromatogram for the experiment with ZG. 42

Figure 5.10 Comparison of peak height between (a) Control-1V, and (b) Control-1S experiments. 44

Figure 5.11 Comparison of peak height between (a) ZG-.025Er experiment, and (b) N_2 injection 45

Figure 5.12 Reactor pressure-time data for control-1V experiment. 45

Figure 5.13 Reactor pressure-time data for experiment with ZG-.025Er sample. 46

Figure 5.14 GC data for Control-3V experiment showing zero hydrocarbon peaks under visible light 46

Figure B.1 Agilent Technologies 7890A GC System. 67

Figure B.2 Agilent Technologies GS-CarbonPLOT capillary column installed in the GC oven. 68

Figure B.3 FID 69

Figure B.4 Bruker D8 ADVANCE diffractometer with a Cu Kα (λ = 0.154 nm) radiation source. 69

Figure B.5 Jasco V-670 UV/VIS Spectrophotometer with a Jasco ISN-723 integrating sphere 70

Figure C.1 Steady state temperature of oil bath and bubbler. 71

Figure C.2 XRD peak search results for ZG-.05Er sample (ICDD PDF-2 2004). 71

ABSTRACT

With an ever-increasing human population, the importance in having sustainable energy resources is becoming increasingly evident, as the current energy habits have brought about massive atmospheric pollution in the form of CO_2 emissions, resulting in a rise in the average global temperature. To battle the effects of climate change, many alternative energy resources have been investigated. Among these, photocatalytic conversion of CO_2 to renewable hydrocarbon fuels such as methane and methanol is one of the most desirable, as it provides the opportunity to utilize the sun's energy to convert CO_2 to renewable fuels. The work in this study is primarily focused on developing a batch photoreactor system to improve the integrity of photocatalytic experiments and using that system to test the performance of Er-doped solid solutions of ZnO/GaN (ZG) towards photocatalytic reduction of CO_2.

To upgrade the abilities from previous photoreactor systems, a novel photoreactor was deigned in SolidWorks and fabricated in-house. The photoreactor was designed to increase surface area at the gas-solid interface, improve utilization of the light source, and promote larger mass transfer rates of reactants to the catalyst surface. These goals were accomplished by immobilizing the catalyst on a transparent porous support, incorporating a threaded mount on top of the photoreactor for mounting an interchangeable LED to illuminate the catalyst bed, and recirculating the gas mixture through a closed loop system with a compressor, respectively.

Pure and Er-doped ZG photocatalyst samples were synthesized through the nitridation of $Zn/Ga/CO_3$ layered double hydroxide (LDH) precursors. Erbium was chosen as a dopant to

potentially enhance the photocatalyst by utilizing its upconversion photoluminescence properties. The LDH precursors were synthesized using a coprecipitation method. Levels of erbium doping were varied by [Er]/[Zn] = 0, 0.025, 0.05, and 0.10. ZnO/GaN solid solutions were chosen for their low bandgap energy so that visible light, roughly 40% of the solar spectrum [1], can be used to activate the catalyst. Diffuse reflectance spectroscopic data of the pure and Er-doped ZG samples were measured and used to calculate the bandgap energy. Bandgap values of E_G = 2.53, 2.52, 2.56, and 2.56 eV were obtained for the [Er]/[Zn] = 0, 0.025, 0.05, and 0.10 samples, respectively. XRD data of the LDH samples indicated the formation of Zn/Ga/CO_3 LDH and the $Zn(OH)_2$, β-Ga_2O_3, α-GaOOH, and $ZnGa_2O_4$ impurity phases. Moreover, the broadening of the diffraction peaks in the Er-doped LDH samples suggested Er^{3+} ions substituted the Ga^{3+} ions in the LDH structure. XRD data of the pure and Er-doped ZG samples revealed strong peaks at 2θ = 31.86, 34.37, and 36.31°, indicating the formation of a solid solution of ZnO and GaN. Additionally, peaks at 2θ = 29.27, 48.79, and 57.86° indicate the formation of the secondary phase of Er_2O_3 in the Er-doped samples. Consequently, it was concluded that the Er^{3+} ions did not go into the crystal structure of the oxynitride solid solution. These findings were supported by the SEM images revealing hexagonal nanoplates and nanoprisms that coincide with the solid solution along with additional nanostructures corresponding to the Er_2O_3 phase.

During photocatalytic experiments with the pure and Er-doped ZG samples, CO_2, and UV light (405 nm nominal wavelength), hydrocarbon production was observed to increase with increasing [Er/Zn]. However, results from control experiments with no catalyst while varying the nominal LED wavelength and the o-ring material suggested that hydrocarbon formation was partially or entirely the result of the o-ring photochemically degrading in the presence of UV light. An o-ring comprised of a silicone material yielded zero hydrocarbon formation in the

presence of UV light, while this was not the case for o-ring materials of Viton® and Kalrez®. These findings can be applied to other research groups that plan to perform photocatalytic experiments in a photoreactor with o-rings while using a UV light source.

CHAPTER 1: INTRODUCTION

1.1 The Human Footprint on the Global Environment

Since the dawn of the industrial age, mankind has made leaps and bounds in technology to benefit humanity. As the number of human inhabitants on earth continues to grow, more and more food and energy resources are required to sustain our ever-increasing population. Fossil fuels have been the most consumed energy resource since the invention of the steam engine due to their abundance and high energy density. However, the combustion of fossil fuels introduces harmful byproducts that have an adverse effect on the global environment. These byproducts, called greenhouse gases, cause the global temperature to rise through a process called the greenhouse effect. Government agencies, such as the Environmental Protection Agency (EPA), enforce regulations on the energy sector to cutback on emissions of greenhouse gases into the atmosphere. However, the EPA currently does not administer any regulations to limit the amount of carbon dioxide (CO_2) emitted into the atmosphere [2]. Thus, the U.S. energy sector continues to blatantly pollute the atmosphere with CO_2 at rates of 5.6 million metric tons per day (2014 levels) [3].

To reduce the amount of CO_2 emitted into the atmosphere, one can either utilize energy resources that emit less CO_2, capture the CO_2 to store it or chemically convert it to something useful, or eliminate CO_2 emissions through the use of clean energy alternatives that have zero CO_2 emissions. Out of these three options, much work has gone into investigating routes towards chemically reducing CO_2 to form hydrocarbon fuels such as methane or methanol. Among the

routes investigated, a process called photocatalysis has sparked interest in the scientific community. This method is especially attractive as it eliminates the need for fossil fuels and closes the carbon cycle. The work presented in this manuscript focuses on testing the performance of photocatalysts towards photocatalytic conversion of CO_2 in a novel batch photoreactor system.

1.2 Photocatalysis and its Applications

Photocatalysis is the process in which energy in the form of light is used to activate a material called a photocatalyst. The photocatalyst increases the rate of a chemical reaction by lowering the activation energy required to initiate the reaction. During the activation step, light absorbed by the photocatalyst excites the material's electrons in the valence band (VB) to a potential energy that is large enough to allow photoexcited electrons to jump to the conduction band (CB). The energy required to excite an electron from the VB to the CB is called the bandgap energy (E_G), or simply the bandgap. The photoexcited electron can then either stay in the CB where it has the chance to reduce nearby chemical species adsorbed to the surface of the photocatalyst, or it can jump back down to the VB to neutralize the overall charge in a process called recombination. Similarly, the positive charge of the vacant electron position in the VB, called a hole, can either oxidize nearby chemical species adsorbed on the photocatalyst surface, or recombine with the photoexcited electron. If reduction takes place in the CB and oxidation has occurred in the VB, the photocatalyst is regenerated and the catalytic cycle begins again.

Photocatalysis can be used in the remediation of pollutants present in wastewater and air. Typically, in photocatalytic wastewater treatment, organic pollutants are degraded into innocuous byproducts through either oxidation by hydroxyl radicals formed by photo-oxidation of water, oxidation by holes at the catalyst surface, or reduction by photoexcited electrons in the

CB [4]. In the remediation of air pollutants, CO_2 is usually the pollutant of most interest. Here, CO_2 is photocatalytically reduced in a multiple electron transfer process that can lead to the formation of various products. Which individual products that form ultimately depends on the number of electrons involved in the specific reaction pathway and the electrochemical potential of the photoexcited electrons and holes [5], [6].

To test the photoactivity of a catalyst towards a specific reaction, multiple experiments are performed in a photoreactor. The data from each experiment is then analyzed and compared to determine if the catalyst is a suitable match for that reaction. Thus, it is critical that the data is scientifically sound to make certain that any and all conclusions made are accurate. In some situations, the arrangement of the photoreactor is of particular interest. In cases such as these, a great deal of effort is made towards designing and building a photoreactor system that yields the most scientifically sound data.

CHAPTER 2: MATERIALS AND CHARACTERIZATION

2.1 Introduction

The majority of semiconductor photocatalysts require UV photons to photoexcite electrons from the VB to the CB. However, UV only makes up roughly 2-5% of the solar spectrum, while about 45% of the spectrum is occupied by visible light and the remaining 50-53% contains near-infrared (NIR) [7], [8]. This disadvantage has lead to continuous efforts by researchers to improve these materials so that they can utilize a greater portion (visible and NIR) of the solar spectrum.

Solid solutions of ZnO and GaN exhibit photoactivity in the visible range of the solar spectrum and have recently been applied towards photocatalytic conversion of CO_2. Wang et al. reported that these materials could be produced using a simple technique involving the low-temperature nitridation of layered double hydroxide precursors [9]. The following two sections of this chapter describe these materials in detail along with the techniques employed to synthesize them.

2.2 Layered Double Hydroxides

Layered double hydroxides (LDH) are a family of materials commonly classified as synthetic anionic clays with brucite-like layers, and take on general formula $[\mathrm{M(II)}_{1-x}\mathrm{M(III)}_x(\mathrm{OH})_2]^{x+}(\mathrm{A}^{n-})_{x/n} \cdot m\mathrm{H_2O}]$. Divalent and trivalent cations (M(II) and M(III), respectively), located in the center of oxygen octahedra, form a positively charged layer that is balanced by an interlayer containing organic or inorganic anionic species [10]. In order to fit in

the octahedral sites, the M(II) and M(III) ions are generally limited to having an ionic radius that lies between that of Be^{2+} and Cd^{2+}[11]. While the divalent and trivalent cations are homogeneously mixed at an atomic scale throughout the cationic layers, the bonding between the host sheets and the interlayer ions are considered to be weak. Implementing an LDH as a precursor is therefore an attractive alternative to traditional materials, as gaseous species can easily diffuse through the interlayer regions and react with the anionic species with minimal additional energy [9].

2.2.1 Synthesis of Zn/Ga/CO_3-LDH

In this study, the M(II) and M(III) ions were Zn^{2+} and Ga^{3+}, respectively, and the interlamellar anion was CO_3^{1-}. A [Zn]:[Ga] atom ratio of 2:1 was employed, as Wang et al. [9] found this composition to yield the most crystalline product with the least amount of secondary phase formation. A coprecipitation technique modified from the procedure described in [9] was utilized to synthesize the Zn/Ga/CO_3 LDH precursors. A nitrate solution containing the M(II) and M(III) cations was formulated by dissolving 2.5385 g of $Zn(NO_3)_2 \cdot 6H_2O$ and 1.1015 g of $Ga(NO_3)_3 \cdot xH_2O$ in DI water. The nitrate solution was then slowly added dropwise to 74.5mL of a 1 M Na_2CO_3 solution. The mother liquor was then aged in the oven at 80˚C for 22hr. After aging, the white precipitate was rinsed with 500mL of DI water in a vacuum filtration flask. The rinsed precursor was then dried in a vacuum oven at 100°C. Once dry, the LDH was ground to a fine powder with a mortar and pestle for no less than 10 minutes.

2.3 ZnO/GaN Solid Solutions

With bandgaps of 3.37 and 3.4 eV, ZnO and GaN, respectively, are both considered wide bandgap semiconductors, meaning that the energy required to excite an electron from the valence band (VB) to the conduction band (CB) is greater than 3.1 eV [12], [13]. Both materials exhibit a

wurtzite crystal structure with similar lattice constants. Therefore, the two semiconductors are able to form a solid solution with the same wurtzite crystal structure. However, not all of the material properties from ZnO and GaN are inherited to the solid solution, as a reduction in the bandgap is noticed in the ZnO/GaN solid solution.

This can be explained by repulsion between p and d orbitals in II-VI semiconductors that leads to an upward shift in VB energy, while the CB energy remains the same. More specifically, it is suggested that p-d repulsion between Zn3d and N2p (or O2p) electrons cause the VB potential energy to shift upward, reducing the bandgap energy [14], [15]. Additionally, it has been found that the bandgap energy is a function of the [Zn]:[Ga] atom ratio, and decreases with increasing Zn concentration [9]. This red shift in the bandgap energy yields a new bandgap in the visible wavelength range, making solid solutions of ZnO/GaN an attractive option as a photocatalyst.

A great deal of research has been dedicated to employing solid solutions of ZnO/GaN in the overall splitting of water into H_2 and O_2 [9], [15]–[17]. The absorption edges of the solid solution are aligned such that oxidation of H_2O and reduction of H^+ are thermodynamically favored [15]. However, recent studies involving ZnO/GaN solid solutions as photocatalysts for conversion of CO_2 have sparked interest in the scientific community. For example, Debusk et al. reported the photoreduction of CO_2 in the presence of ZnO/GaN powders decorated with 5 wt% Ru. A yield of 43.3 nmols of CO was achieved after 380 minutes of UV irradiation [18].

Yu et al. tested the photocatalytic activity of various ZnO/GaN samples loaded with Rh, Cr, Ni, and Mg. No hydrocarbon evolution was noticed during experiments with the samples decorated with Ni/NiO and Rh/Cr core-shell structures. However, samples impregnated with Rh

and Mg showed activity on the photocatalytic conversion of CO_2 to methanol at a rate of 0.78 μmol g^{-1} h^{-1} [19].

Samples of pure ZnO/GaN have also shown photoactivity in the conversion of CO_2. A recent study by Zhou et al. investigated the use of pure ZnO/GaN nanotubes as a photocatalyst for CO_2 conversion [20]. An enhancement in photoactivity towards methane production was noticed in the nanotube samples (0.072 μmol g^{-1} h^{-1}) when compared to the nanoparticle samples (0.033 μmol g^{-1} h^{-1}). The authors attributed this effect to a higher specific surface area in the nanotube samples and a reduced length in the carrier diffusion path through the nanotube walls.

Table 2.1 Comparison of rates of photocatalytic reduction of CO_2.

Material	Light Source	Major Product	R_{max}	Ref.
ZnO/GaN nanotubes	300 W Xe arc lamp with filter (λ>420 nm)	CH_4	0.072 μmol g^{-1} h^{-1}	[20]
ZnO/GaN nanotubes	300 W Xe arc lamp (UV-VIS)	CH_4	0.60 μmol g^{-1} h^{-1}	[20]
ZnO/GaN nanoparticles	300 W Xe arc lamp with filter (λ>420 nm)	CH_4	0.033 μmol g^{-1} h^{-1}	[20]
ZnO/GaN powders with 5 wt% Ru	400 W tubular Hg lamp (UV)	CO	0.068 μmol g^{-1} h^{-1}	[18]
ZnO/GaN impregnated with Rh and Mg	300 W Xe lamp with VIS filter	CH_3OH	0.78 μmol g^{-1} h^{-1}	[19]
TiO_2–P25	60 W daylight bulb (λ=400-850 nm)	CH_4	0.5 μmol m^{-2} h^{-1}	[21]
TiO_2–P25	100 W Hg vapor lamp (λ=365 nm)	CH_4	~1.97 μmol m^{-2} h^{-1}	[21]
TiO_2 (anatase)	75 W high-pressure Hg lamp (λ>280 nm)	CH_4	0.03 μmol g^{-1} h^{-1}	[22]

Due to its photoactivity in visible light and the recent advances in its application to photocatalytic conversion of CO_2, pure and Er-doped ZnO/GaN solid solutions and their photoactivity towards CO_2 photoreduction were investigated in this study.

2.3.1 Doping with Rare-Earth Metal Ions

One promising technique to utilize visible and NIR sunlight is the doping of semiconductors with rare-earth metal ions. These rare-earth metal ions have multiple energy states that allow the conversion of low-energy photons (NIR and vis) to photons of higher energy via a process called upconversion luminescence [23]. In this process, a low-energy photon (visible or IR) absorbed by a rare-earth metal ion excites an electron from ground state to a higher energy state. This electron then decays to an intermediate energy level between ground state and the first excited energy level. Then, a second low-energy photon is absorbed and excites the electron to transition to a higher energy level. The ion then relaxes and undergoes a transition from an excited state to the ground state, during which a photon of higher energy (UV) is emitted.

Applying this process to a semiconductor doped with rare-earth metal ions gives the upconverted photon a chance to excite an electron in the VB of the semiconductor to the CB. However, it is important to note that this upconverted photon must have energy greater than or equal to the bandgap energy of the semiconductor to produce an electron-hole pair. Furthermore, not all rare-earth metal ions exhibit this characteristic. It has been found that this phenomenon only occurs in trivalent metal ions from the Lanthenide group, as these elements have multiple energy states due to their large d orbitals.

In this study, samples of ZnO/GaN solid solutions doped with various amounts of erbium were synthesized in the lab using the same procedure as the non-doped samples. A total of four doped samples were synthesized, where the quantities of the erbium dopant, introduced in the form of $Er(NO_3)_3 \bullet 5H_2O$ during the LDH synthesis, were varied with respect to the quantity of

zinc in the samples. A list of the samples and their corresponding erbium to zinc ratio ([Er]/[Zn]) and mass of $Er(NO_3)_3 \cdot 5H_2O$ are given in Table 2.1.

Table 2.2 Mass of $Er(NO_3)_3 \cdot 5H_2O$ in LDH samples.

Type of Catalyst	Sample Name	Mass of $Er(NO_3)_3 \cdot 5H_2O$ (g)
ZnO/GaN-[Er]/[Zn]=0	ZG	0
ZnO/GaN-[Er]/[Zn]=.025	ZG-.025Er	0.1890
ZnO/GaN-[Er]/[Zn]=.05	ZG-.05Er	0.3772
ZnO/GaN-[Er]/[Zn]=.10	ZG-.10Er	0.5676

2.4 Synthesis of ZnO/GaN Solid Solutions

To form the ZnO/GaN solid solution, the LDH was nitrided under flow of anhydrous NH_3 at 300 mL/min in a tube furnace. First, the white LDH powder was placed into a ceramic combustion boat and carefully loaded into the tube furnace. The tube furnace was then capped with Swagelok Ultra-Torr fittings on both ends and the temperature program was loaded. During the ramping portion of the temperature program, dry inert N_2 was flowed through the tube furnace to ensure there was no oxidation of the LDH. Once the furnace reached 800°C, the flow was switched from N_2 to NH_3. After 30 minutes, the flow was switched back to N_2 and the furnace was left to cool down to room temperature. Finally, the nitrided powder was then removed from the tube furnace and weighed on a digital scale.

2.5 Characterization

2.5.1 Powder X-ray Diffraction

All LDH and ZnO/GaN samples synthesized in the lab were characterized by a Bruker D8 ADVANCE diffractometer with a Cu Kα ($\lambda = 0.154$ nm) radiation source to generate X-ray diffraction (XRD) patterns. The LDH samples were scanned from 10˚ to 70˚ 2θ, and the

ZnO/GaN samples were scanned from 20˚ to 80˚ 2θ. The XRD data for all samples was compared to those found in literature.

2.5.2 Diffuse Reflectance Spectroscopy

Diffuse reflectance spectra (DRS) data was collected for all ZnO/GaN samples using a Jasco V-670 UV/VIS Spectrophotometer equipped with a Jasco ISN-723 integrating sphere attachment. Light from the halogen lamp light source was shined onto the sample and diffuse-reflected light was detected from 700 to 300 nm with a 0.5 nm step size by the photomultiplier tube (PMT) detector. A Spectralon® standard reflection plate was used as a reference to perform a baseline correction. The DRS data was then sent through a MATLAB program for analysis.

2.5.2.1 MATLAB Bandgap GUI

A MATLAB program was developed to estimate the optical bandgap of semiconductors using DRS data and the Kubelka-Munk radiative transfer model. The program allows the user to interactively locate and upload the DRS data file and specify parameters associated with the semiconductor. The resulting output from the program is a Tauc plot of $(h\nu F(R_\infty))^{1/n}$ versus $(h\nu)$, where h is Planck's constant, ν is the light frequency, $F(R_\infty)$ is the remission function of Kubelka-Munk, and n is a constant that takes on different values based on the mode of electronic transition for the semiconductor. The bandgap is estimated by locating the x-intercept of the line tangent to the point of inflection and is displayed on the figure window along with the Tauc plot. Refer to Appendix A for the MATLAB programs used in this study.

2.5.3 BET Surface Area

Brunauer–Emmett–Teller (BET) surface area measurements were performed on ZnO:GaN samples A and B using a Quantachrome Autosorb-iQ Gas Sorption System.

2.5.4 Scanning Electron Microscopy

The surface morphology of LDH sample A and ZnO:GaN samples A through D was elucidated by a JEOL JSM-7500F field emission scanning electron microscope (SEM). The images were captured using an acceleration voltage from 1 to 2 kV. To reduce the landing energy of the electron beam and improve the image resolution and contrast [24], a stage bias (SB) voltage of 0 kV for sample A of the LDH and ZnO:GaN and -2 kV for ZnO:GaN samples B through D were applied to the specimen. All samples were secured to the stage via carbon tape.

CHAPTER 3: PHOTOREACTOR DESIGN

3.1 Motivation

In the process of attaining reliable data from a gas-phase photocatalytic experiment, it is necessary to have control of the process variables that alter the validity of the acquired data. These process variables include: temperature, pressure, partial pressures of reactants, light intensity and wavelength, flow rate (if a flow-through system is used), and the gas-solid interfacial surface area. Having control over these variables requires a robust system that facilitates reproducible results. The systems that were used for previous studies in our lab were lacking in controllability of these important process variables.

Results from scientific research are limited in value by the veracity of the measurements taken and the data acquired. Therefore, it is important to conduct experiments in a manner such that the apparatus allows the user to correctly quantify the measurements taken. This was the driving force that led us into designing a system that minimizes the effects of the following sources of discontinuity in experimental data:

1. Exposure of photocatalyst to light
2. Catalyst loading technique
3. Macroscopic mass-transfer limitations

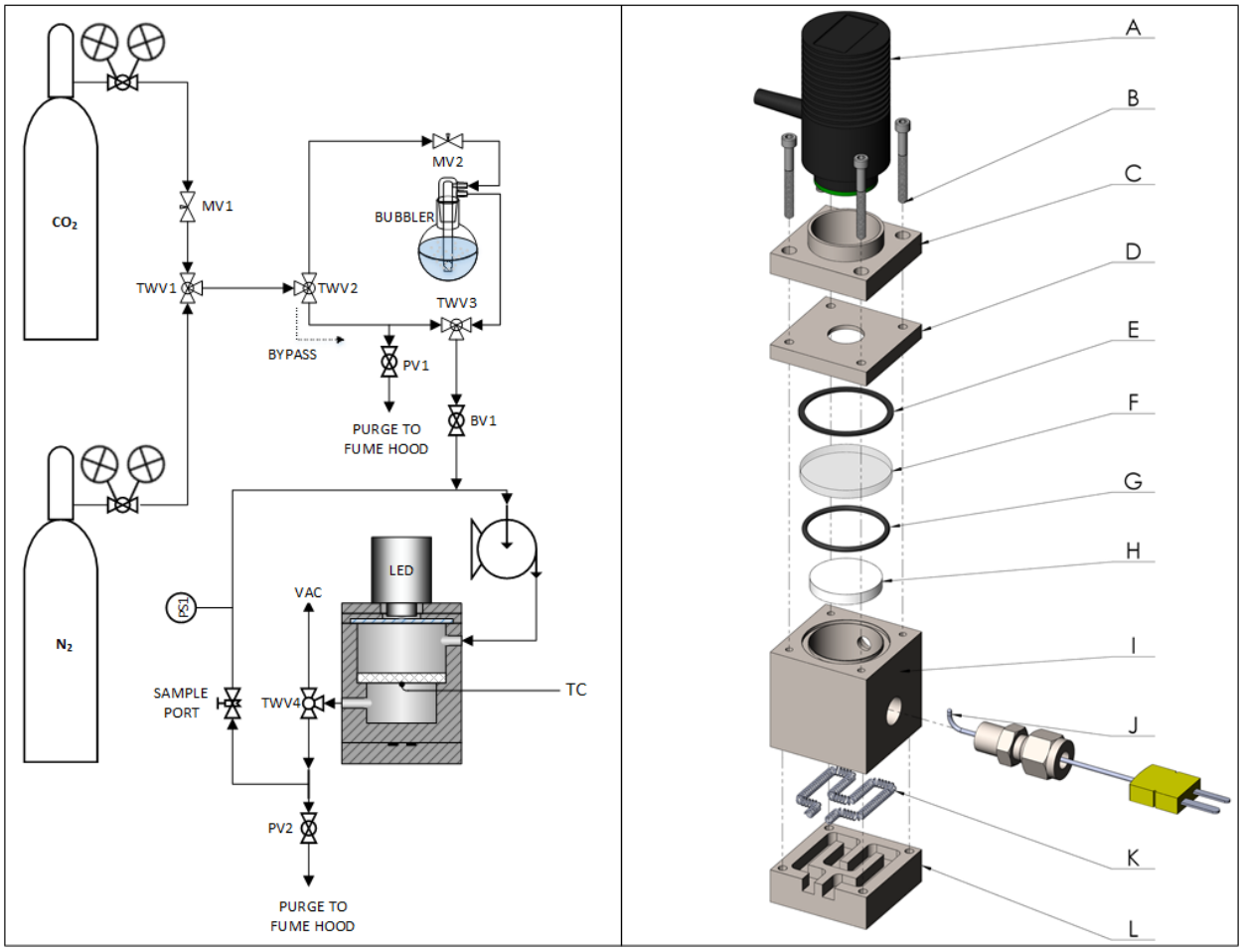

(a) (b)

Figure 3.1 Photoreactor P&ID and exploded drawing.

3.2 Reactor Cell

The photocatalytic reactions take place in the reactor cell where the photocatalyst is irradiated by the light source and is in contact with the reaction mixture. Machined out of chemically resistant 316 stainless steel, the reactor has a maximum oxidation service temperature of 870°C in air and can endure harsh and corrosive environments. A 1.000-inch diameter counterbore at 0.580 inches deep and a 0.950-inch diameter pilot hole at 1.140 inches deep were machined into the center of the cell by a CNC mill. The bottom of the counterbore acts as a shelf for holding the catalyst bed. The counterbore depth was predetermined with the goal of having the light source focused on the catalyst bed so that it is completely illuminated while limiting the

amount of light illuminating the reactor cell walls. This was accomplished by using a combination of Snell's law and the viewing angle of the LED light source. The diagram in Figure 3.2 below illustrates how the distance between the catalyst bed and quartz window was calculated.

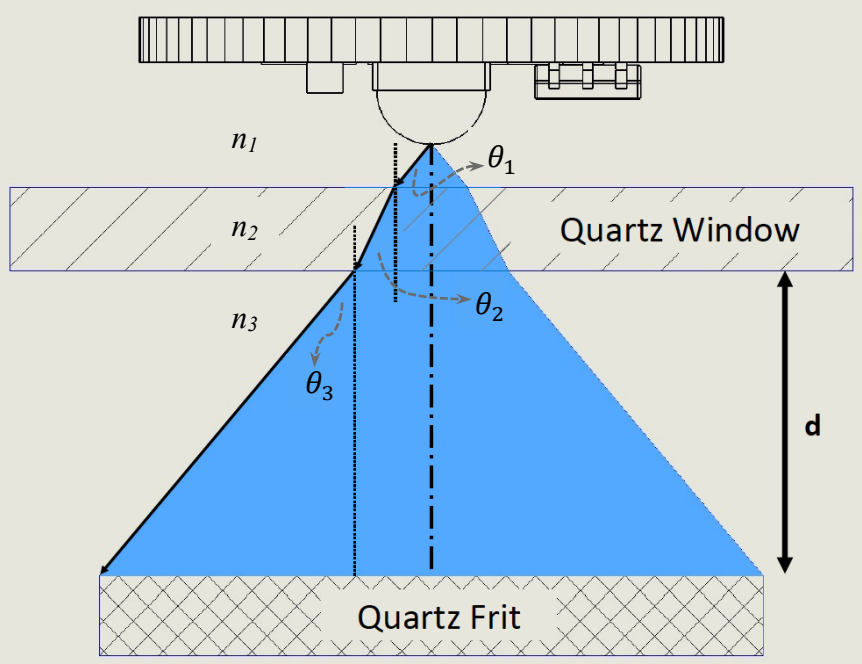

Figure 3.2 Diagram showing how the window-bed distance was determined.

3.3 Catalyst Bed

One of the main objectives in designing a new photoreactor was to utilize the catalyst more efficiently by incorporating a sample holder that increases its exposure to light and the reaction mixture. This was achieved by immobilizing the photocatalyst onto a porous catalyst bed to allow the reaction mixture to flow through the support and react with the catalyst. A quarter-inch thick fritted glass filter with a 25 mm diameter was used as the catalyst bed due to its high porosity and transparency. The glass frit was purchased from Adams & Chittenden Scientific Glass and has a P0 standard porosity designation. Frits that are designated by the P0

porosity have pore sizes that range from 160 to 250 microns and have a pore volume of roughly 35%.

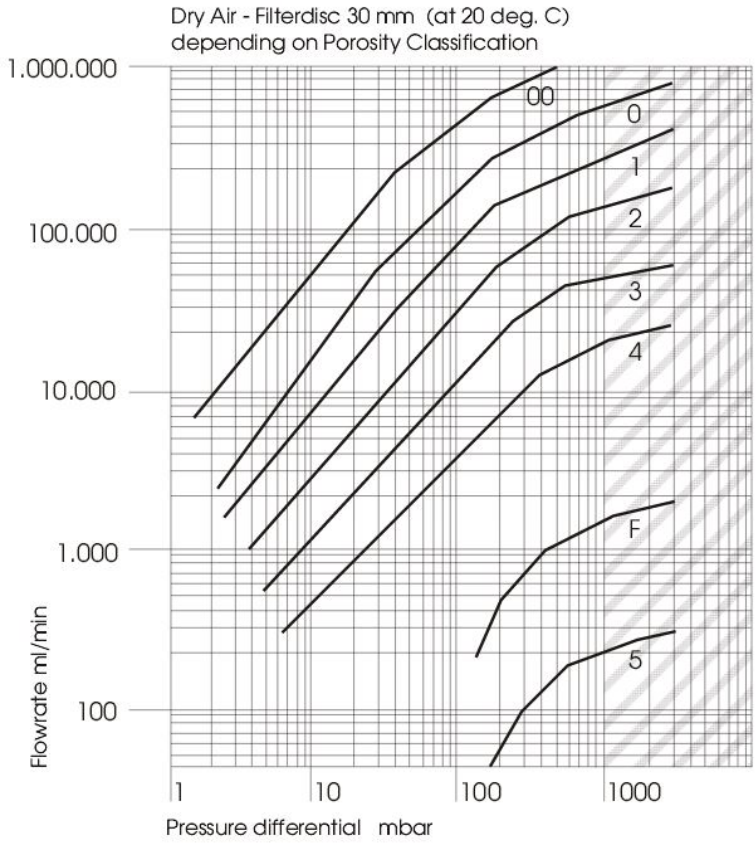

Figure 3.3 Flow-pressure chart for fritted glass filters of various standard porosity ratings.

3.4 Irradiation Source

The most straightforward approach to effectively compare the reactivity of various photocatalysts is to calculate the photonic efficiency, or apparent quantum yield (ζ), using the easily obtained number of photons entering the photoreactor (I_0) and the rate of reaction:

$$\zeta = rate/I_0(\lambda) \tag{3.1}$$

The apparent quantum yield becomes more valuable when the amount of light that is absorbed by the photoreactor is minimized and the amount of light irradiating the catalyst bed is maximized. Ideally, all of the light from the irradiation source should completely cover the catalyst bed and should not protrude over the boundaries of the optical window or to the interior

walls of the photoreactor. However, since the irradiation source is typically located outside of the photoreactor, the light must travel through an optical window. Consequently, photons have the chance to be absorbed by the optical flat before they reach the photocatalyst.

To ease the process of calculating the quantum efficiency, time was taken to design a photoreactor that allows the user to quantify the flux of photons incident on the photocatalyst. This was accomplished by including a threaded light mount in the design where an interchangeable LED light source directly mounts to the photoreactor just above the optical window.

3.4.1 Interchangeable Mounted LED

The light source used in this study is a single LED purchased from Thorlabs with a nominal wavelength of 405 nm and mounted to the end of an aluminum heat sink (see Figure 3.4 for the LED spectrum). The heat sink is equipped with 6 mm-long internal SM1 (1.035”-40) optical threads for allowing easy mounting and dismounting from other optical components. The LED is shown as the part labeled ‘A’ in Figure 3.1 Photoreactor P&ID and exploded drawing (b). To power the LED, a 12 V analog LED driver with a manual control knob was purchased from Thorlabs.

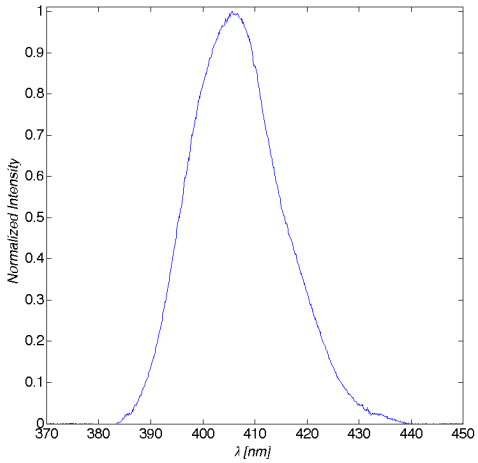

Figure 3.4 Spectrum of Thorlabs M405L2 LED.

3.4.2 Threaded LED Mount

A threaded light mount was constructed to secure the LED to the photoreactor in a position that allows the light path to completely cover the catalyst bed. As shown in Figure 3.1 Photoreactor P&ID and exploded drawingb and Figure 3.5, the light mount is installed to the top face of the trap flange. Both mating faces of the light mount and the trap flange assemble flush so that no light from the LED is able to leak out from between the two components. Similar to the internal threads of the heat sink, the external threads of the mount are SM1 (1.035”-40) optical threads. When the LED is completely fastened to the light mount, the tip of the LED primary lens sits 1/32” above the reactor window. The light mount was fabricated from 316 stainless steel in the engineering machine shop located on campus.

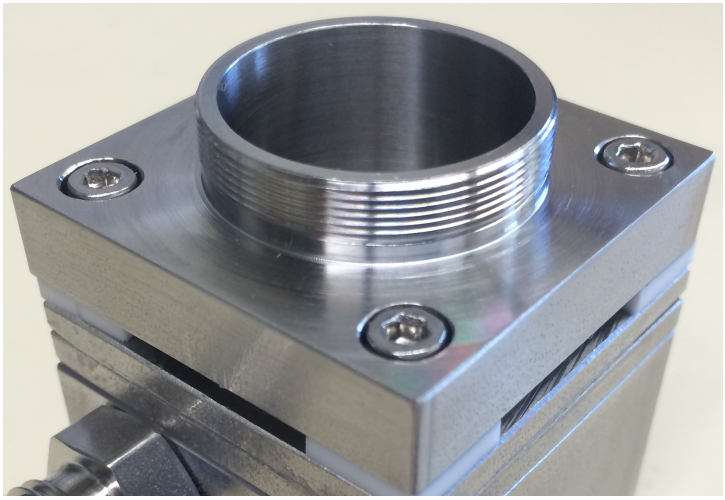

Figure 3.5 Threaded mount for interchangeable LED.

3.5 Gas Delivery System

To introduce gases to the reactor, a gas delivery system (GDS) consisting of plumbing for a bubbler and a bubbler bypass was fabricated. As illustrated in the P&ID for the photoreactor system in Figure 3.1 Photoreactor P&ID and exploded drawinga, inlet gases are directed to either the bubbler or the bubbler bypass by three-way valve 2 (TWV2) located at the inlet of the GDS.

At the outlet of the GDS, TWV3 diverts flow from either the bubbler or the bubbler bypass to the reactor.

3.5.1 Bubbler

The bubbler consists of a 500 mL Pyrex boiling flask with a thermometer well and a fritted gas-washing stopper. A 125 X 65 mm Pyrex crystallizing dish filled with heat stabilized silicone fluid was used as an oil bath for the boiling flask. The temperature of the boiling flask was measured and controlled indirectly by a thermocouple submerged in the silicone fluid and connected to a (Corning PC-420D) hot plate stirrer controller.

After measuring the steady state temperature difference between the oil bath and boiling flask, it was found that the average temperature offset between the two was 4˚C. Therefore, the temperature set point at the hot plate controller was set to 4˚C above the desired bubbler temperature. The steady state temperature data for the oil bath and boiling flask can be found in Figure C.1 Steady state temperature of oil bath and bubbler..

3.5.2 Bubbler Bypass

For gases that do not need to pass through the bubbler, plumbing for a bubbler bypass was fabricated and installed to the GDS. To clear the bypass lines of N_2 during the CO_2 charging procedure, a purge valve was installed in the bypass plumbing. This ensures that pure CO_2 is used during the charging step. The purge valve is labeled as PV1 in Figure 3.1a.

3.6 Recirculating Flow

Another issue encountered in previous batch photoreactor systems is external mass-transfer limitations. Reaction rate data reported for systems with these limitations is undesirable, as the rate of reaction is limited by the rate of transfer of reactants from the bulk fluid phase to the surface. This leads to a lower overall rate of reaction, ultimately translating to longer

experiment times. The general procedure for photocatalytic experiments involves loading the catalyst into the reactor, charging the reactor with a gaseous reaction mixture, and then allowing the system to equilibrate before shining light on the catalyst to initiate the reaction. Previous batch photoreactor systems in our lab did not employ a means of forced convection to recirculate the reaction mixture. Therefore, the reaction mixture was stagnant and molecular diffusion was the dominating mode of mass-transfer, as bulk motion of the fluid by natural convection was minimal.

To further illustrate how molecular diffusion by means of a concentration gradient and the bulk motion of the fluid contribute to the total molar flux, the following equation for the molar flux of species A, W_A, is defined below:

$$W_A = J_A + B_A \tag{3.2}$$

where J_A is the molecular diffusion flux of A generated by a concentration gradient, and B_A is the flux of A as result of bulk motion of the fluid. For a binary mixture of A and B, the molecular diffusion flux of A, J_A, in a three-dimensional system can be described using Fick's first law:

$$J_A = -D_{AB}\nabla C_A \tag{3.3}$$

where D_{AB} is the diffusivity of A in B, and C_A is the molar concentration of A. The flux of A by the bulk motion of the fluid B_A can be described in terms of the molar average velocity V:

$$B_A = C_A V \tag{3.4}$$

Substituting equations (3.3) and (3.4) into equation (3.2), we obtain a final expression for the molar flux of A:

$$W_A = -D_{AB}\nabla C_A + C_A V \tag{3.5}$$

Applying the above expression to the reaction mixture inside the photoreactor, we find that the molar flux of reactants from the bulk fluid phase to the catalyst surface increases with

the bulk velocity [25]. In our system, this is achieved by recirculating the reaction mixture through a closed recirculation loop with a compressor to facilitate mass-transfer of reactants to the surface of the catalyst.

3.6.1 Metal Bellow Compressor

An MB-21 Senior Aerospace metal bellow compressor was chosen to recirculate the reacting media through the reactor and plumbing of the closed recirculation loop. The bellows are made from corrosion resistant AM 350 stainless steel, while the valve assembly gaskets are Teflon. The compressor is rated to handle media temperatures up to 80˚C during continuous operation. This relatively low maximum media temperature is the result of the class B insulation for keeping the motor below its maximum operating temperature of 41˚C. The estimated flow rate of the recirculating reaction mixture at atmospheric pressure was found to be around 0.2 scfm. This was found by referring to flow-pressure chart in Figure 3.6 and finding the flow of air at a pressure of 0 psig for the MB-21 model. Using this flow rate and the flow-pressure chart for the P0 frit in Figure 3.3, it was then determined that the differential pressure across the glass frit is estimated to be 4.5 mbar.

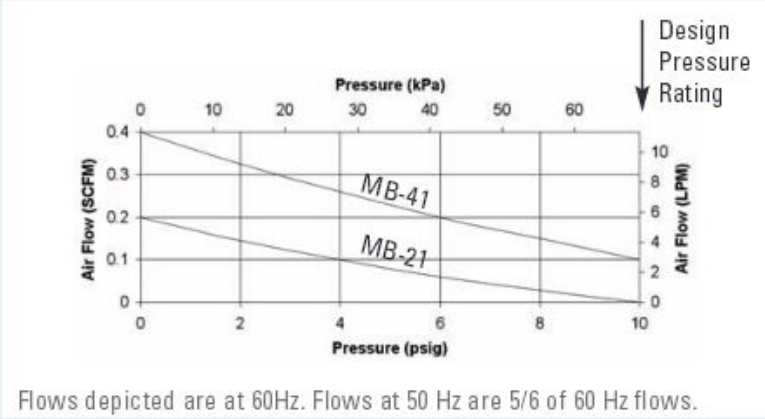

Figure 3.6 Flow-pressure chart for MB-21 metal bellow compressor.

Figure 3.7 MB-21 metal bellow compressor.

3.6.2 Recirculation Loop

To recirculate the reaction mixture, a closed loop plumbing system connecting the photoreactor and compressor was fabricated out of quarter-inch stainless steel tubing. This closed recirculation loop (CRL) has one inlet and two outlets. In Figure 3.1a, BV1, the ball valve between the GDS and CRL, charges the reactor when opened and isolates the reactor when closed. To flush the system of air and any potential contaminants remaining from previous experiments, plumbing for a purge line (PV2) and an in-house vacuum line were connected to the recirculation loop. A three-way valve (TWV4) connects the recirculation loop to the photoreactor outlet and the in-house vacuum line and allows the user to evacuate the reactor plumbing down to a pressure of about 10 Torr. PV2 is used to vent gases from the photoreactor system to a fume hood through polyethylene tubing.

To keep the water vapor in the reactor system from condensing, heat tape and insulation were installed on the CRL plumbing and the plumbing of the bubbler outlet. The temperature of the tubing's exterior surface was monitored with a type k thermocouple, and controlled manually by adjusting a 120 V variable voltage transformer to which the four strands of heat tape were connected.

3.7 Integrated Heating Element

To provide heat to the photoreactor, an integrated heating element was fabricated. The heating element, comprised of a 316 stainless steel body with a groove for holding a resistance heating wire, is mounted to the bottom of the reactor cell by four socket head cap screws. The resistance heating wire is encased in a ceramic sleeve to electrically isolate it from the stainless steel body. Tin plated copper ring terminals were spot-welded and crimped at either end of the heating wire to connect the heater to a terminal block where a temperature controller connects to supply the heater with power.

3.7.1 Resistance Heating Wire

The resistance heating wire is a nickel-chromium alloy of 60% nickel, 16% chromium, and balance iron. The nickel-chromium wire, or nichrome, was manufactured by OMEGA and arrives precoiled in a spool. Per manufacturer recommendations, the precoiled wire was extended to three times the spooled length before sleeved and installed into the wire groove. Thus, the precoiled length of the nichrome wire cut from the spool was $1/3^{rd}$ the length of the groove path, which was taken as the center line lengths in the CAD drawing shown in Figure 3.8b.

3.7.2 Heating Element Body

Wire grooves were machined into the heating element body to guide the nichrome wire along a path that allows uniform heating of the reactor cell. The groove width and depth were dimensioned to allow 1/32” of extra space above, below, and on either side of the nichrome wire to make room for the ceramic sleeving. CAD drawings of the heating element body are shown in Figure 3.8.

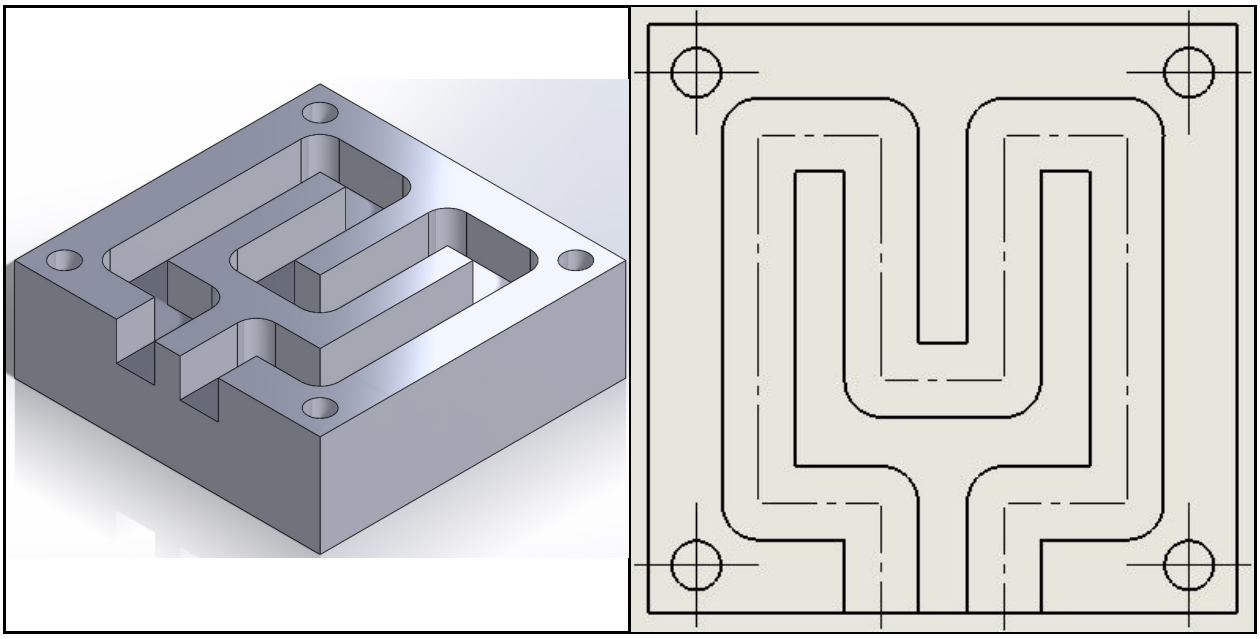

(a) (b)

Figure 3.8 CAD drawings of heating element body.

3.7.3 Heating Element Temperature Controller

To automatically control the reactor cell temperature, a temperature controller was constructed in the lab. The controller consists of a 1/16 DIN temperature controller mounted in an aluminum enclosure. Inside the enclosure, the temperature controller is connected to a solid-state relay (SSR) that controls a 120V AC load from the 5V DC controller output. A fast blow fuse connected between the SSR output and the load protects the controller circuit from overloading. To turn the controller circuit on and off, a rocker switch was mounted to the front panel of the enclosure and connected between the load and the SSR output to open and close the controller circuit. The controller input is a female type K thermocouple connector mounted on the rear panel of the enclosure.

3.8 Hermeticity

In order to assure that changes in measured reactant and product concentrations are the result of a chemical reaction rather than the result of a leak in the photoreactor system, time was

spent to design a system that is hermetically sealed. Possible locations where leaks could occur are at the window-o-ring interface, the reactor inlet and outlet, and within the CRL plumbing. Leaks from within the CRL plumbing were mitigated with ease using Swagelok® compression fittings. Our approach to addressing the remaining two possible sources for leaks is presented in the following two sections.

3.8.1 O-Ring Assembly

An o-ring located between the quartz window and reactor cell body keeps the photoreactor gas-tight. To maintain internal pressure, the outer diameter of the o-ring groove was set equal to the outer diameter of the o-ring. This allows the pressurized media inside the reactor cell to push the o-ring to the outer wall of the o-ring groove, forming the airtight seal. An o-ring having a standard size of dash number 023 was used, as this size was found to fit best with the photoreactor cell dimensions. The o-ring groove dimensions for the dash number 023 o-ring were designed according to the design tables for static o-ring face seal glands in the Parker O-Ring Handbook[26]. To further illustrate how the trap flange, window and gasket, and o-ring are assembled, an exploded view of a cross-section of the reactor cell is shown in Figure 3.9 below.

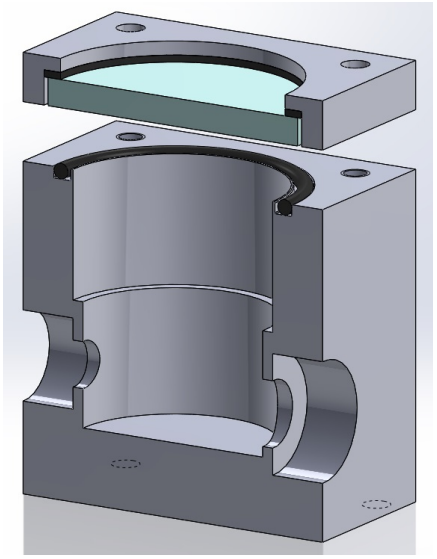

Figure 3.9 Exploded view of a cross-section of the reactor cell.

3.8.2 Inlet and Outlet Connectors

Welded connections were used at all three of the reactor ports to mitigate the possibility of leaks. Three counterbore holes were machined to the reactor cell at three separate external faces for male pipe weld connectors. Countersinks were placed at the entrance of the holes to create a groove channel and trap the molten filler material close to the connector, creating a finer weld bead. All three connectors transition from male pipe weld connectors to compression tube-fittings. Two of the connectors are used as means of evacuating the chamber and introducing gases through inlet and outlet ports (Figure 3.10a), while the other connector is used to embed a $1/16^{th}$-inch stainless steel sheathed K-type thermocouple for measuring the temperature of the catalyst bed (Figure 3.10b).

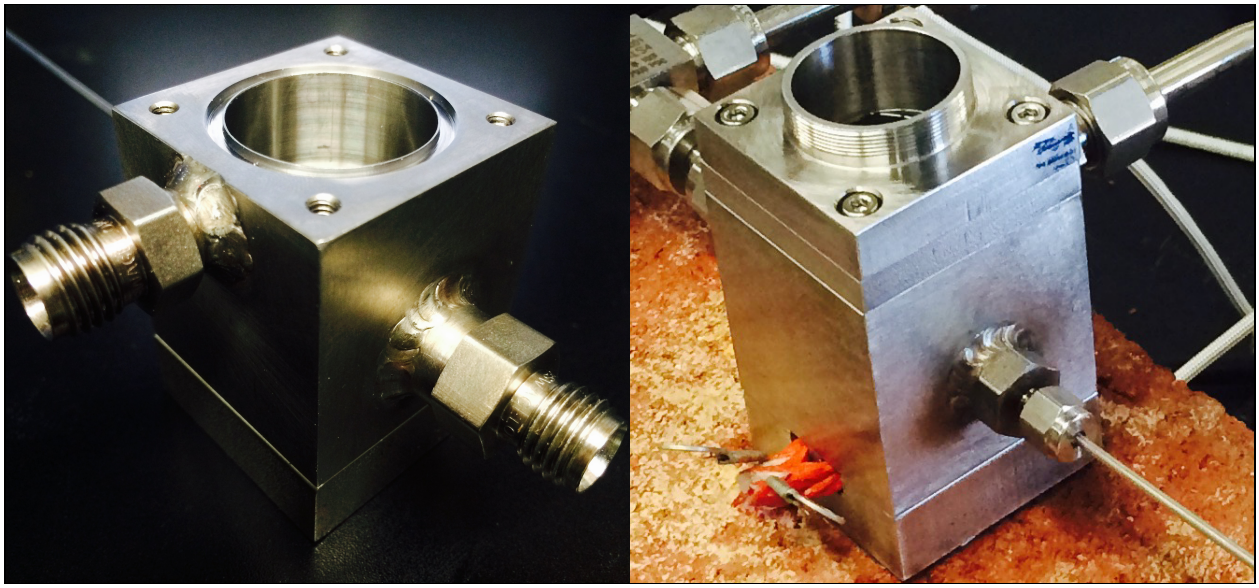

(a) (b)

Figure 3.10 Images of welded pipe weld connectors for (a) the reactor inlet and outlet, and (b) thermocouple.

CHAPTER 4: PHOTOCATALYTIC EXPERIMENTS

4.1 Design of Experiments

Prior to conducting the photocatalytic experiments in this study, all of the major input factors in a single experiment were identified. Input factors that were directly tunable were defined as process variables, while the remaining input factors were noted as being process constants. From these input factors, an experimental matrix was formulated to organize how the process variables would vary for each experiment. For the sake of time and simplicity, the experiments were designed so that only one process variable would be varied while the rest were held constant. It was decided that the process variable to vary between experiments, or the independent variable, would be the photocatalyst.

Along with the pure and Er-doped ZG samples, TiO_2 (Degusa P25) was also tested in the photoreactor and was used as a reference since it is a widely studied material. Additionally, two control experiments were performed to confirm the validity of data that suggest CO_2 was photocatalytically converted. The first control experiment was conducted to verify that the formation of hydrocarbons was the result of a photocatalytic reaction rather than the photochemical degradation of carbonaceous compounds present in the photoreactor or photocatalyst. This was accomplished by running an experiment with no catalyst and with the UV LED turned on.

A second control experiment was carried out to investigate if any hydrocarbon formation was the result of thermal decomposition of carbon-containing reactor components, such as o-

rings, gaskets, or organic contaminants in the photocatalyst. This was achieved by conducting an experiment with TiO_2 and with the LED turned off.

Due to the inherent variability in the photoreactor system, actual values of process variables were expected to have some degree of deviation from their set point. Values of process variable set points and process constants for each experiment are presented in the form of an experimental design matrix in Table 4.1. The actual values of the process variable set points and process constants can be found in Table C.2.

Table 4.1 Experimental design matrix with values of process variables and constants.

Exp. #	Catalyst	T_B (°C)	T_R (°C)	m_{cat} (g)	LED_P (%)	P_{R1} (Torr)	P_{R2} (Torr)	λ (nm)	t_{RXN} (h)	t_{SPL} (h)
1	-	31.5	45	0	100	760	767	405	4	1
2	P25	31.5	45	0.02	0	760	767	405	4	0.5
3	P25	31.5	45	0.02	100	760	767	405	4	0.5
4	ZG	31.5	45	0.02	100	760	767	405	4	0.5
5	ZG-.025Er	31.5	45	0.02	100	760	767	405	4	0.5
6	ZG-.05Er	31.5	45	0.02	100	760	767	405	4	0.5
7	ZG-.10Er	31.5	45	0.02	100	760	767	405	4	0.5

4.2 Startup Procedures

4.2.1 Cleaning

Prior to all photocatalytic experiments, steps were taken to prepare the apparatus for experiments. The first of these steps was cleaning any of the photoreactor components that directly contact the reaction mixture, including the reactor cell, window assembly, o-ring, and glass frit. The window assembly and o-ring were first rinsed with deionized (DI) water to remove any loose debris, then soaked and scrubbed in a cleaning solution containing DI water,

isopropanol, and Sparkleen™ detergent. To remove any samples left on the catalyst bed from previous experiments, the glass frit was sonicated repeatedly for two-minute cycles in the same cleaning solution described above, replacing the cleaning solution between each cycle until no further clouding of the cleaning solution was observed. All photoreactor components were then rinsed with DI water and dried under vacuum at 100˚C for 10 to 15 minutes.

4.2.2 Sample Preparation

To prepare the samples for photocatalytic experiments, the glass frit was first placed on the shoulder of the counterbore in the reactor cell. Then, the photocatalyst was carefully shoveled from a piece of weighing paper into a pile at the center of the glass frit. The sample was then spread evenly onto the glass frit by using a lab spatula in an outward spiraling motion, dispersing the catalyst until it formed a uniform layer. Once evenly spread, the photocatalyst was compressed into a cake-like disk by pressing it with the bottom of a 10 mL glass beaker. An image of a ZG sample loaded in the photoreactor cell is shown in Figure 4.1.

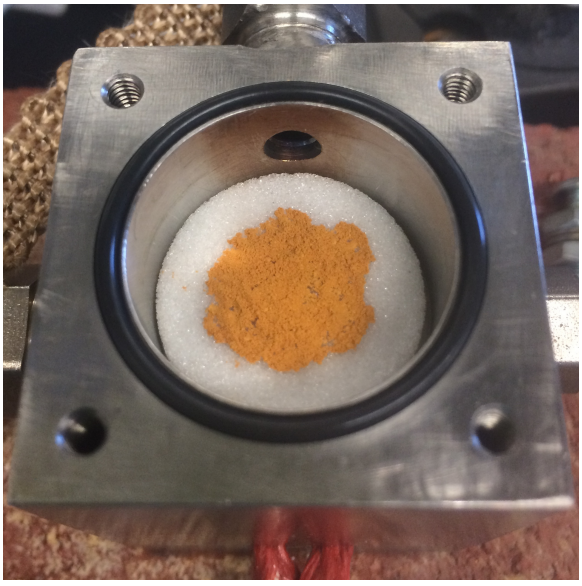

Figure 4.1 Image of a ZG sample loaded in the photoreactor cell.

4.2.3 Purging the Reactor

Due to the presence of dead end cavities, undesired gases in the CRL and photoreactor were eliminated using a vacuum-assisted cycle purging procedure that uses the combination of in-house vacuum to evacuate undesired gases, and ultra high purity nitrogen (Airgas 99.999%) to replace undesired gases with an inert gas[27]. First, the BV1 and PV2 were closed before switching TWV4 to allow the system to be evacuated by in-house vacuum. After the system was opened to in-hose vacuum, the compressor was briefly switched on to allow any undesired gases in the metal bellow to be evacuated. Once the pressure sensor readout indicated that the rate of pressure change decreased to about -0.5 Torr per minute, TWV4 was switched back to isolate the CRL from in-house vacuum.

Before pressurizing the CRL with N_2, the compressor was turned off to ensure that the motor was not subjected to too much strain. Then, TWV1, TWV2, and TWV3 were switched to divert N_2 flow to the CRL, and BV1 was opened to charge the system with 5 psig of N_2. The compressor was then turned back on to circulate N_2 and BV1 was closed to isolate the CRL. After recirculating N_2 for about thirty seconds, the compressor was turned off and the CRL was opened to in-house vacuum to start the vacuum assisted cycle purging procedure once again. This process was repeated sixty times.

4.2.4 Introducing Nitrogen and Water Vapor

The CRL and photoreactor were charged with a N_2 mixture saturated with water vapor using a similar iterative procedure to the purging procedure described in the previous section. However, the CRL was not evacuated during this step. To introduce the water-saturated N_2 mixture to the CRL, TWV1, TWV2, and TWV3 were switched to divert N_2 flow through the bubbler and to the CRL. With the PV2 closed and the system isolated from in-house vacuum,

BV1 was then opened and the compressor was turned on. At this point, the nitrogen-water mixture was circulating through the CRL.

Once the pressure of both the N_2 supply and the CRL had reached equilibrium, indicated by the absence of bubbles in the boiling flask, PV2 was opened to vent the system to atmospheric pressure for about thirty seconds. Then, PV2 was closed and the procedure was repeated for thirty cycles. After the 30^{th} cycle, BV1 was closed, immediately followed by PV2. The pressure of the CRL was considered atmospheric during this step, as PV2 was the last valve to close, which vents atmospheric pressure. Finally, the pressure and temperature of the CRL, P_R and T_R, respectively, and the temperature of the bubbler, T_B, were recorded.

4.2.5 Charging CO_2

Before introducing CO_2 to the system, the bubbler bypass was cycle purged with CO_2 by opening PV1 thirty times to ensure that only pure CO_2 was charged to the system. After purging, with PV1 left open, the CO_2 delivery pressure was set to 5 psig and the regulator outlet valve was just barely opened. Then, the CO_2 low flow metering valve at the GDS inlet was closed, immediately followed by the bypass purge valve. BV1 was then opened, immediately followed by MV1 set to a low-flow valve setting to enable more control of CO_2 pressure. Once the reactor pressure sensor readout indicated that the desired final pressure had been reached, BV1 was closed and the final reactor pressure was recorded. Finally, the system was left alone for 15 minutes in dark conditions to allow the adsorption and desorption of gases to reach equilibrium.

The pressure of CO_2 to be charged to the reactor was determined by a molar ratio of H_2O:CO_2 of 5:1. A spreadsheet was written to calculate the required pressure of CO_2 to be added to the system to achieve the desired molar ratio using the reactor temperature, reactor pressure, and bubbler temperature as input variables. After the values for the input variables were entered

in the spreadsheet, the photoreactor and CRL were charged with the required pressure of CO_2. For a more detailed explanation on the spreadsheet used in this study, refer to appendix b.

4.3 Photocatalytic Reaction Procedures

Once the system had reached equilibrium, the first 200-μL sample was taken via syringe through a septum and the reactor temperature and pressure were recorded. At that point, the data points taken were considered the initial state of the reaction. That is, the initial concentration, initial reactor temperature, and initial reactor pressure at time equals zero. Each sample was injected into the split/splitless inlet of the GC for analysis (refer to Appendix B: Instrumentation for a detailed description of the GC setup). Next, the LED was turned on to full power and a timer for thirty minutes was started for the next sample to be taken. This procedure was repeated an additional eight times for a total of four hours of light exposure and nine sets of data.

4.4 Shutdown Procedures

Later, after the last sample had been taken, the LED was turned off and the reactor was cycle purged with in-house vacuum and N_2 once again to remove reaction products and water vapor from the system, as exposing the interior surface of the metal bellow compressor to moisture for extended periods of time can lead to corrosion[28]. After closing BV1, PV2, and TWV4, the compressor was turned off while leaving on all of the heat tapes and the hot plate stirrer.

CHAPTER 5: RESULTS AND DISCUSSION

5.1 Powder X-Ray Diffraction

The XRD data of the pure and Er-doped LDH precursors (Figure 5.1a) showed similar diffraction patterns, which display the distinctive features of a triple layered hexagonal cell [9], [29]. However, the diffraction peaks were broadened with an increasing value of [Er]/[Zn], indicating that interstitial impurities could be causing local deviations in the d-spacings, resulting in non-uniform distortions in the lattice structure [30]. This discovery could imply that Er^{3+} is substituting Ga^{3+} at the M(III) site within the oxygen octahedra. Moreover, additional peaks in the pure and Er-doped LDH diffraction patterns at 2θ = 12.7, 19.6, 26.8, and 36.5° signify the existence of multiple impurity phases including $Zn(OH)_2$, β-Ga_2O_3, α-GaOOH, and $ZnGa_2O_4$, respectively [9], [29], [31].

For the pure and Er-doped ZG samples, the XRD patterns indicated that nitridation of the LDH precursors provoked the formation of the secondary Er_2O_3 phase. This is uncovered by the peaks located at 2θ = 29.3, 48.8, and 57.9°. After comparing these 2θ values to those that came up in a peak search from the peak diffraction file database (Figure C.2), it was confirmed that these extra peaks are from Er_2O_3. This implies that the Er^{3+} ions were oxidized during the nitridation step. Since the atmosphere during the nitridation procedure is NH_3, it can be assumed that either the neighboring hydroxyl groups in the oxygen octahedra, or the CO_3^{2-} anions in the interlayers of the LDH oxidized the Er3+ ions.

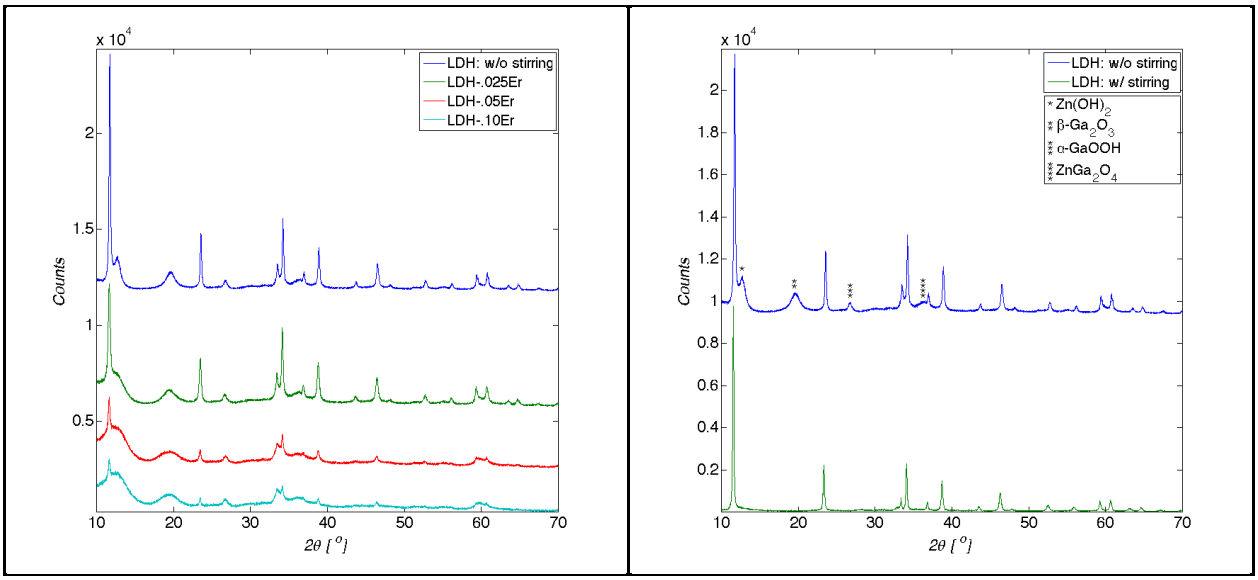

(a) (b)

Figure 5.1 XRD data for (a) all LDH samples and (b) LDH with and without stirring.

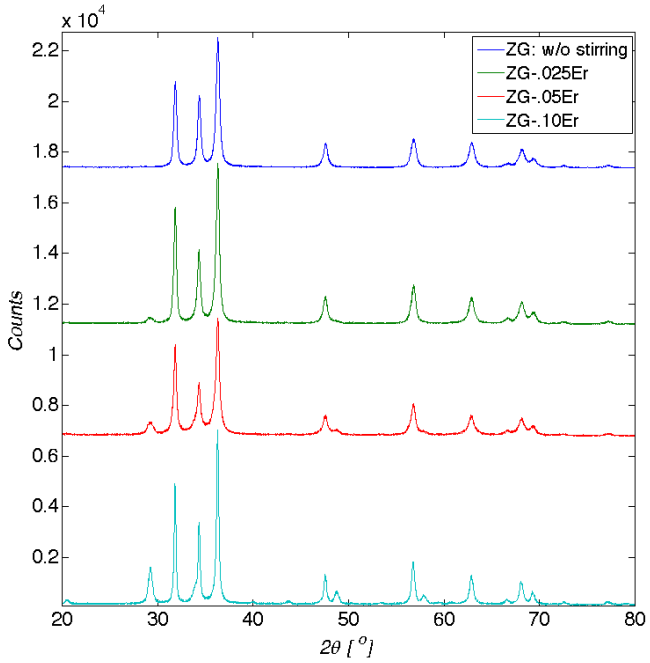

Figure 5.2 XRD data for the nitrided ZG samples.

The crystallite sizes of the pure and doped LDH and ZG samples were estimated using the Scherrer equation (Table 5.1). It should be noted that many factors contribute to the observed diffraction peak profile. These contributions are a combination of both instrument and sample-dependent effects. For the sake of simplicity, the effects of the instrumental profile on peak

broadening were considered negligible. Moreover, sample-dependent effects include microstrain and crystallite size. However, only the crystallite size effects on peak broadening were considered.

In the pure and Er-doped LDH samples, the craystallite size was observed to decrease with increasing [Er]/[Zn], with the LDH sample having a calculated crystallite diameter of 39.61 nm and the LDH-.10Er sample having a calculated crystallite diameter of 3.41 nm. This was, however, not the case for the pure and Er-doped ZG samples, as the crystallite size was found to increase with increasing erbium content. This can possibly be explained by the formation of a more crystalline ZG product upon nitriding the LDH precursor. Additionally, the formation of the secondary phase of Er_2O_3 after nitriding the LDH can give reason to why peak broadening is observed in the diffraction peaks of the erbium-doped LDH samples. It is possible that the peak broadening in these samples is the result of lattice strain or microstrain in the form of point defects, such as the interstitial or substitution of atoms. For example, the Er^{3+} cation could substitute the Ga^{3+} cation at the M(III) site in the center of the oxygen octahedra, causing a local deviation of d-spacings from the average value.

Table 5.1 Calculated crystallite sizes for the pure and Er-doped LDH and ZG samples.

Sample	Phase	Crystallite Size* [nm]
LDH	$Zn/Ga/CO_3$	46.99
	β-Ga_2O_3	8.07
LDH-.025Er	$Zn/Ga/CO_3$	39.80
	β-Ga_2O_3	7.34
LDH-.05Er	$Zn/Ga/CO_3$	31.02
	β-Ga_2O_3	3.72
LDH-.10Er	$Zn/Ga/CO_3$	6.70
	β-Ga_2O_3	3.72
ZG	ZnO/GaN	29.98
	Er_2O_3	–
ZG-.025Er	ZnO/GaN	33.18
	Er_2O_3	18.12
ZG-.05Er	ZnO/GaN	34.16
	Er_2O_3	14.81

Table 5.1 (Continued)

Sample	Phase	Crystallite Size* [nm]
ZG-.10Er	ZnO/GaN	47.68
	Er_2O_3	28.18

An additional batch of the LDH sample was synthesized to explore the affects of stirring during the precipitation step of the synthesis. In this second batch, the Na_2CO_3 solution was stirred with a magnetic stirrer while the nitrate solution was added dropwise. After comparing the XRD data between the LDH samples with and without stirring (Figure 5.1b), it was noticed that stirring during the precipitation step results in a single phase product with no impurities and is more compliant with XRD data from literature [9]. One possible explanation for this occurrence is that stirring the solution changes the relative rates of crystallization and nucleation in favor of crystallization. Stirring would also increase the rate at which Ga^{3+} and Zn^{2+} migrate to the oxygen octahedral sites, which would lead to larger LDH crystallites. In other words, stirring the solution during the precipitation step could increase the rate of crystallization and decrease the rate of nucleation, resulting in a product that is higher in crystallinity and more homogeneous while decreasing the probability of impurity phases forming.

5.2 Diffuse Reflectance Spectroscopy

The calculated bandgaps of the pure and Er-doped nitrided samples were acquired by uploading the DRS data to the MATLAB GUI and is tabulated in Table 5.2. An example of what the GUI output (the Tauc plot) looks like is shown in the Figure 5.3 below. The red line in this plot represents the line tangent to the point of inflection of the Kubelka-Munk function. The value of the x-intercept of this straight line is taken to be the estimated bandgap, E_G, of the semiconductor. The value of n, representing the mode of electronic transition, was chosen to be

0.5, as it is stated in literature that solid solutions of ZnO/GaN exhibit direct allowed electronic transitions [32].

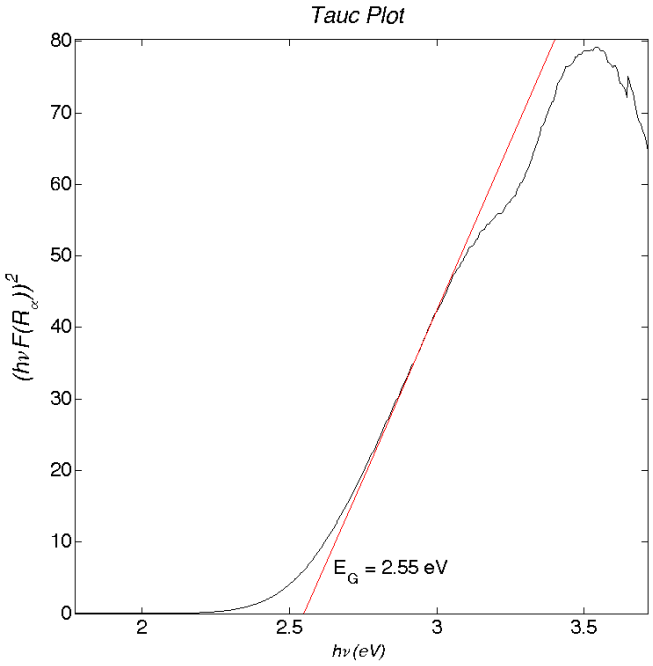

Figure 5.3 Tauc plot for the pure ZG sample.

The DRS data for the erbium-doped samples shows two dips in reflectance that straddle 657 nm. This agrees with absorption spectra data for oxidized erbium, Er_2O_3, found in literature [33]–[35] and can be attributed to a transition from $^4I_{15/2}$ to $^4F_{9/2}$.

Table 5.2 Calculated bandgaps for the pure and Er-doped ZG samples.

Sample	[Er]/[Zn]	E_G (eV)
ZG	0.00	2.55
ZG-.025Er	0.025	2.52*
ZG-.05Er	0.05	2.56
ZG-.10Er	0.1	2.56

*E_G value is averaged over two samples

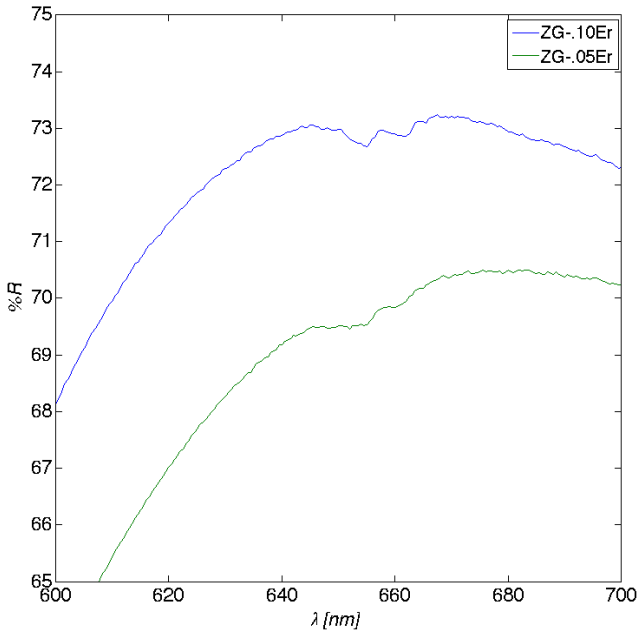

Figure 5.4 Zoomed in reflectance spectra for samples ZG-.10Er and ZG-.05Er.

5.3 BET Surface Area

The specific surface areas for the ZG and ZG-.025Er samples were calculated via the Brunauer-Emmett-Teller (BET) method. This data, along with the pore volume, is given in Figure 5.5. A slight increase in specific surface area was noticed when comparing the ZG-.025Er sample (14.7 m^2/g) to the ZG sample (14.4 m^2/g). It is believed that this is the result of the introduction of erbium leading to the formation of the secondary phase of Er_2O_3. This claim is qualitatively supported by the morphology of the Er-doped ZG samples in the SEM images and semi-quantitatively supported by the smaller crystallite sizes of the Er_2O_3 phase calculated from the XRD data.

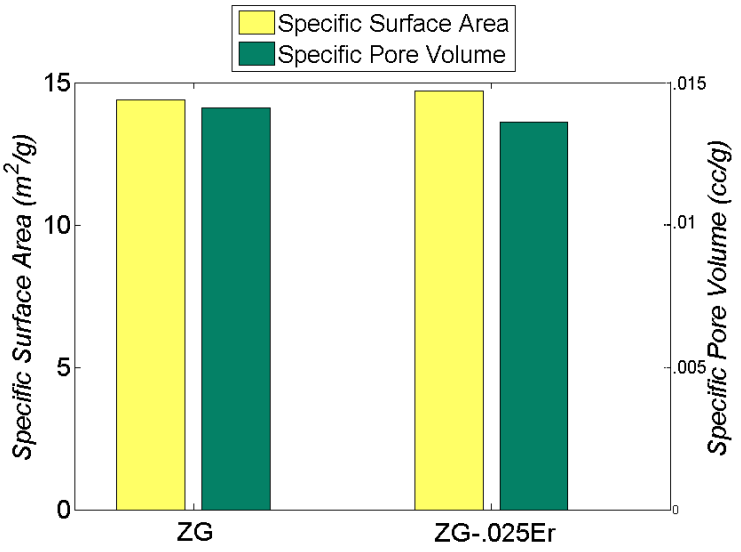

Figure 5.5 N_2 Physisorption results for samples ZG and ZG-.025Er.

5.4 Scanning Electron Microscopy

SEM images (Figure 5.6) reveal that the surface morphology of the as-prepared pure and Er-doped ZG samples contain hexagonal nanoplates with an average diameter of about 210 nm and other nanostructures. The nanoplates can be attributed to the wurtzite structure of the ZnO:GaN solid solutions. The other nanostructures, attributed to the Er_2O_3 phase, are not clearly defined to a single shape due the relatively low resolution of the SEM images. The nanoplate structures were found to become less apparent as the erbium content was raised. The Er_2O_3 nanostructures were found to become more prominent with an increasing erbium content, supporting the finding from the XRD data.

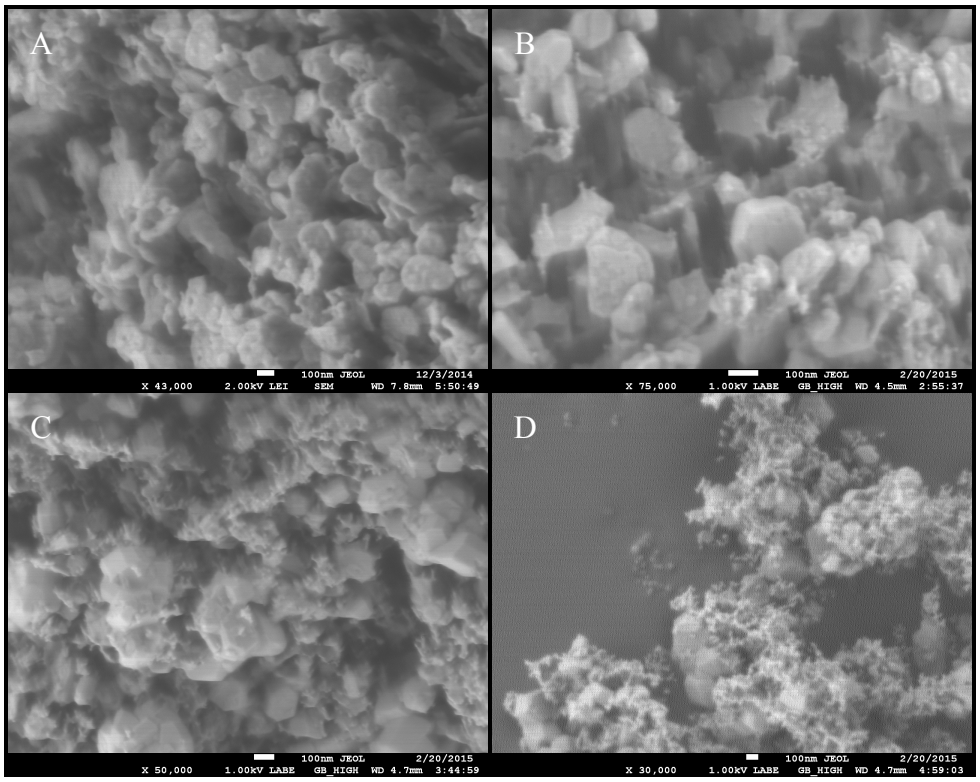

Figure 5.6 SEM images revealing the morphology of (a) ZG, (b) ZG-.025Er, (c) ZG-.05Er, and (d) ZG-.10Er

5.5 Energy Dispersive X-Ray Spectroscopy

To give insight on the elemental composition, EDS data were acquired for the LDH, ZG, and ZG-.025Er samples and is tabulated in Table 5.3 below. According to this data, the measured values of [Zn]/[Ga] and [Er]/[Zn] vary significantly from their predicted values. This variability can be attributed to many factors that include, but are not limited to, analytical error and the synthesis procedure. Possible sources of analytical error include the technique used for background correction, and the normalization of EDS results in standardless analysis of a non-standard material. In the case of analytical error stemming from background correction, uncertainties may arise for relatively low concentrations at lower beam voltages as a result of poor line energy separation, overlapping of peaks, and a higher background at these low energies [36]. For example, the detection of nitrogen is shown to be at a beam voltage less than 1 keV in

the EDS spectrum for the ZG sample (Figure 5.7). Generally, the EDS background tends to rise at beam voltages less than 1 keV. Thus, depending on how the background data is subtracted, a false mass fraction value can be calculated.

In the case of errors stemming from the synthesis procedure, it is highly likely that the measured quantities of the nitrates during the synthesis of the LDH precursors do not contain the theoretical amount of Er^{3+}, Zn^{2+}, and Ga^{3+} ions. This is because nitrate salts are hygroscopic and will grab ahold of atmospheric water vapor if they are exposed to humid air. Even though the stock bottles of all nitrates used in this study were stored in a vacuum desiccator when not being used, they were exposed to the humid air during the weighing step. It is possible that this short period of time that the nitrates were exposed to the humid air was enough to significantly alter the composition of the salts to the point where the composition of the LDH precursors were affected.

Table 5.3 EDS data for the LDH, ZG, and ZG-.025Er samples.

Sample	Wt% C	Wt% O	Wt% N	Wt% Zn	Wt% Ga	Wt% Er	[Zn]/[Ga]	[Er]/[Zn]
LDH	35.2	23.7	–	28.6	12.6	–	2.8	–
ZG	–	10.2	0	68.7	21.2	–	3.5	–
ZG-.025Er	–	14.2	0	58.3	22	5.5	2.8	0.037

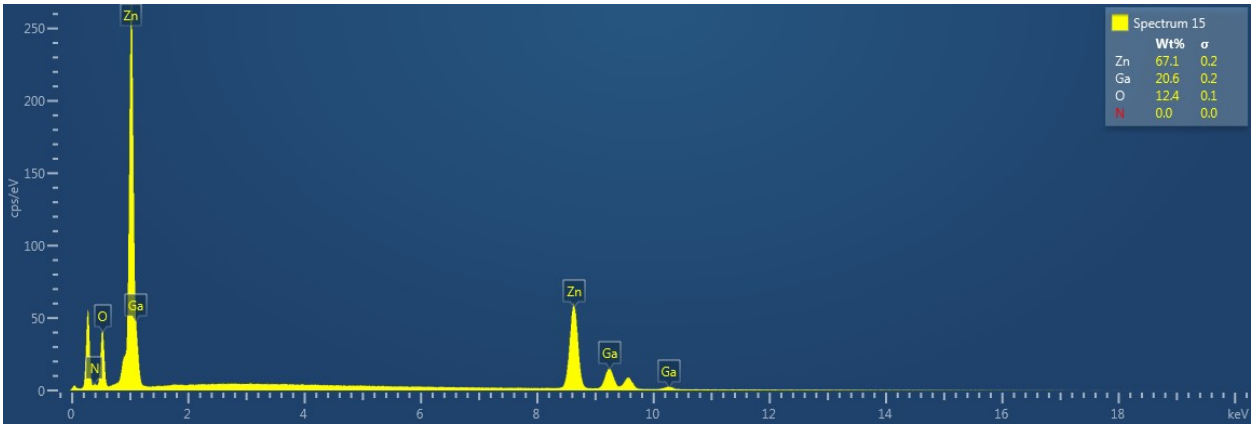

Figure 5.7 EDS spectrum for the ZG sample.

5.6 Photocatalytic Experiments

Photocatalytic experiment data was collected and analyzed via gaseous syringe injection into the split inlet of the GC. To compare to a well-studied material, P25-TiO_2 was loaded into the reactor. The evolution of a peak having a retention time of about 2.65 minutes was noticed for all experiments. However, the area of the peak in the GC data for the experiment with TiO_2 (Figure 5.8) was noticeably larger than that of the experiments with ZG samples and the doped counterparts.

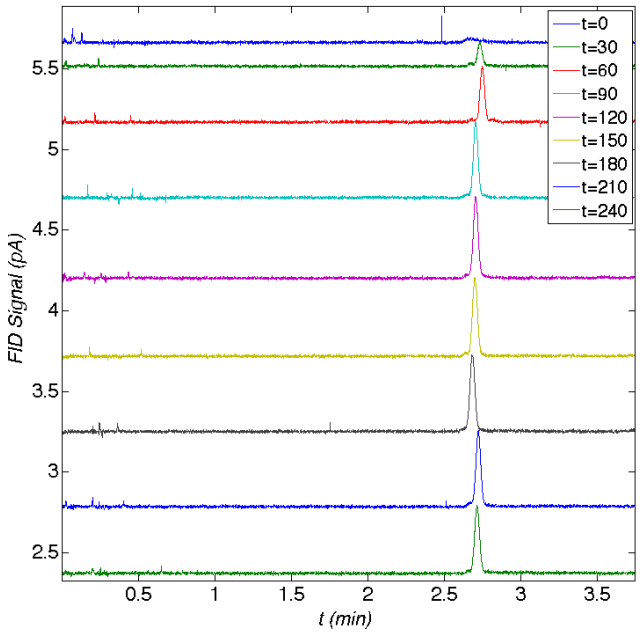

Figure 5.8 Chromatogram for the experiment with TiO_2.

The GC data from the photocatalytic experiments with the pure and Er-doped ZG samples were analyzed to check for the formation of gaseous hydrocarbons. While the experiment with the ZG sample showed essentially no hydrocarbon peaks in the GC data (see Figure 5.9), the GC data for the experiments with Er-doped samples suggested the formation of hydrocarbons occurred during the photocatalytic experiments. Out of all of the ZG and doped samples, the greatest hydrocarbon yield was achieved with the ZG-.025Er sample, with a final

peak height of 0.3696 pA above the baseline of the FID signal (Figure 5.11a). However, the reactor pressure data for the photocatalytic experiments were erratic in comparison to that of the control-1V experiment, as seen in Figure 5.13 and Figure 5.12, respectively. It was later discovered that the septum installed in the Ultra-Torr fitting for taking samples via syringe had a leak and caused the random nature of the reactor pressure. After installing a new septum, the reactor pressure began to behave in a more regular manner in the control-1V experiment by steadily decreasing with each sample taken (Figure 5.12).

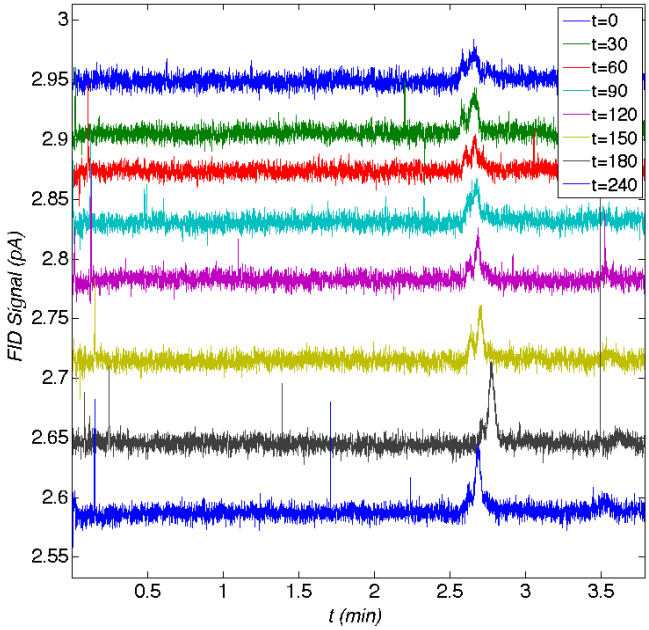

Figure 5.9 Chromatogram for the experiment with ZG.

The control experiments without catalyst and with UV light produced a peak in the FID signal with the same retention time as the peak from the experiments with a catalyst. This suggests the formation of hydrocarbons may be the result of either a photocatalytic reaction with the gas mixture and the photocatalyst, or a reaction with some component within the photoreactor apparatus, or a combination of the two. To further investigate the source of this inherent hydrocarbon evolution, control experiments with varying light sources, gas mixtures,

and o-ring materials were performed. The parameters for these control experiments are given in the Table 5.4 below.

Table 5.4 Control experiment parameters.

Experiment	O-Ring Material	Light Source	Gas Mixture
Control-1V	Viton®	UV (405 nm)	N_2, H_2O, CO_2
Control-1K	Kalrez®	UV (405 nm)	N_2, H_2O, CO_2
Control-1S	Silicone	UV (405 nm)	N_2, H_2O, CO_2
Control-3V	Viton®	VIS (530 nm)	N_2, H_2O, CO_2
Contol-4V	Viton®	UV (405 nm)	N_2

The formation of hydrocarbons was found to depend strongly on the light source and o-ring material. This was discovered in the experiment with visible light, Viton® o-ring material, and a gas mixture of H_2O, CO_2, and N_2. In this experiment, no hydrocarbon peaks were noticed (see Figure 5.14), which suggests that UV light was playing a role in the hydrocarbon formation. It was then later proposed that the o-ring was photochemically degrading in the presence of UV light by means of a light-induced radical reaction at the surface of the elastomer o-ring. In an attempt to test this hypothesis and improve the integrity of the reactor system for UV light experiments, additional o-ring materials were tested in the presence of UV light and a gas mixture of CO_2, H_2O, and N_2.

One of those materials was Kalrez®, or perfluoroelastomer. Kalrez was chosen for its high maximum operating temperature and outstanding chemical resistance properties. However, despite these desirable properties, hydrocarbon peaks were still noticed when testing Kalrez in the presence of UV light and the gas mixture mentioned above. This can be explained by the fact that both Viton® and Kalrez® are primarily composed polymers and copolymers with carbon-carbon bonds which are relatively easy to break in the presence of UV light and form highly unstable radical intermediates.

In an attempt to eliminate this possibility, a silicone o-ring material was tested. This control experiment yielded essentially zero hydrocarbon formation in 90 minutes. When comparing the FID signal after 90 minutes of exposure to UV light in the control experiments with silicone and Viton®, it is apparent that the latter o-ring material photochemically degrades in the presence of UV light, while the former o-ring material proves to be resistant to photochemical degradation. This is shown in Figure 5.10 where the peak height for the Viton® control experiment is larger than that of the silicone control experiment by a factor greater than 21.

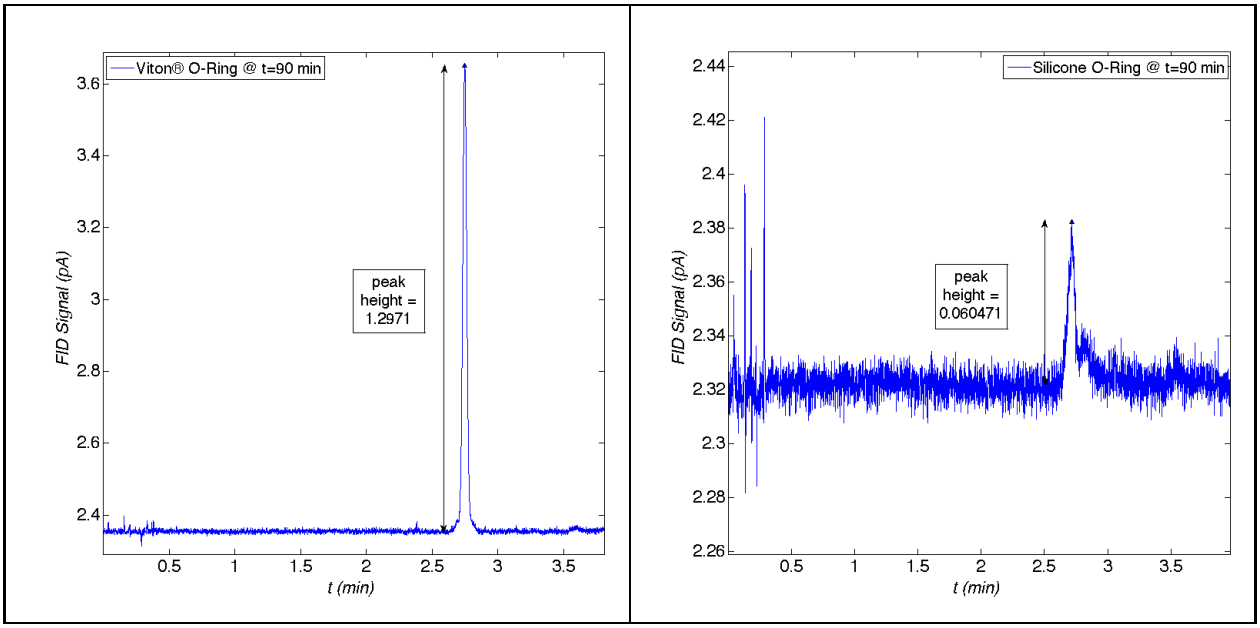

(a) (b)

Figure 5.10 Comparison of peak height between (a) Control-1V, and (b) Control-1S experiments.

It should be noted that a rise in FID signal was detected upon injection of non-hydrocarbon samples, such as air and N_2. This rise in signal occurred at the same retention time as the hydrocarbon peaks detected in the photocatalytic experiments. However, the difference in peak height and baseline is significantly less than that of the peaks present in the photocatalytic experiments. This can be shown by making a comparison between the chromatogram for an injection of pure N_2 and the chromatogram at the 4-hour mark of the experiment with the ZG-

.025Er sample, shown in Figure 5.11. The peak height in (a) is larger than that of (b) by a factor greater than 9. With this notion, it was assumed that the rise in FID signal by N_2 within the sample is negligible.

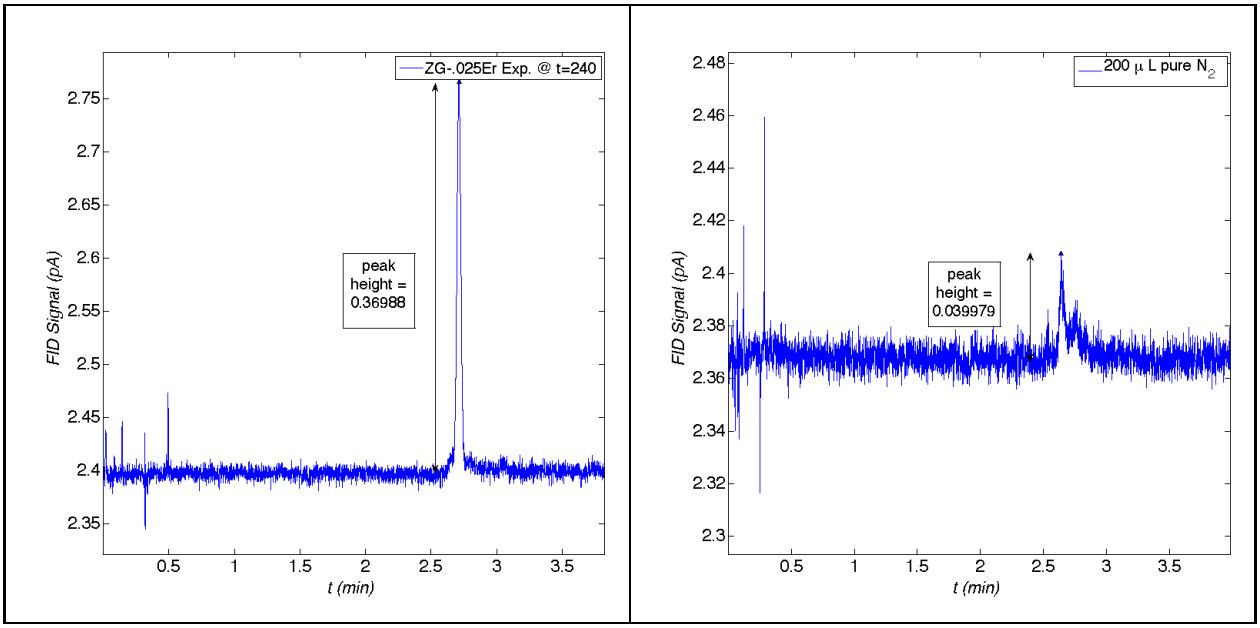

(a) (b)

Figure 5.11 Comparison of peak height between (a) ZG-.025Er experiment, and (b) N_2 injection.

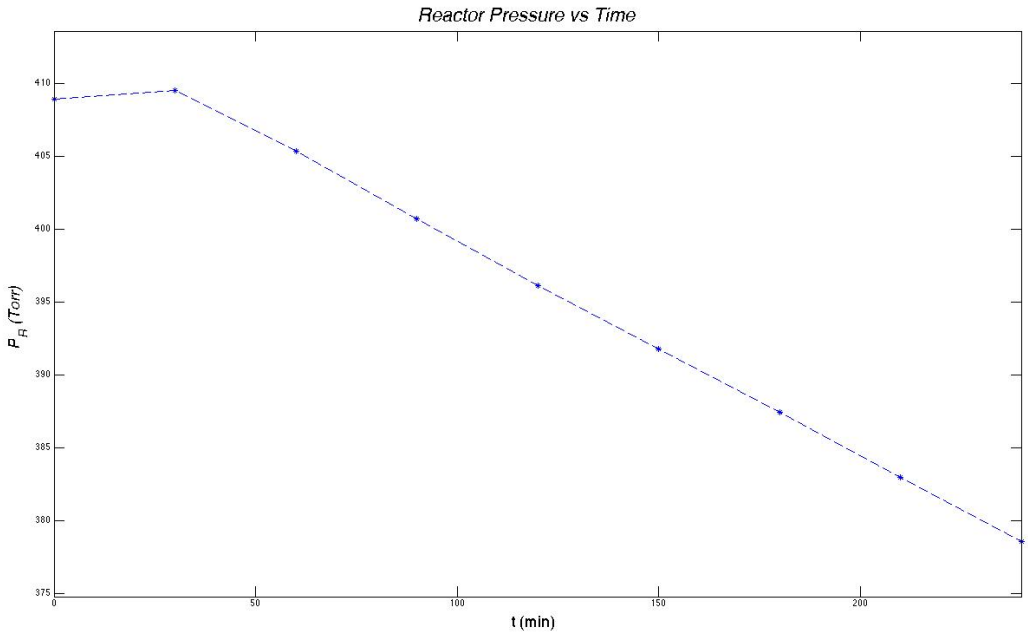

Figure 5.12 Reactor pressure-time data for control-1V experiment.

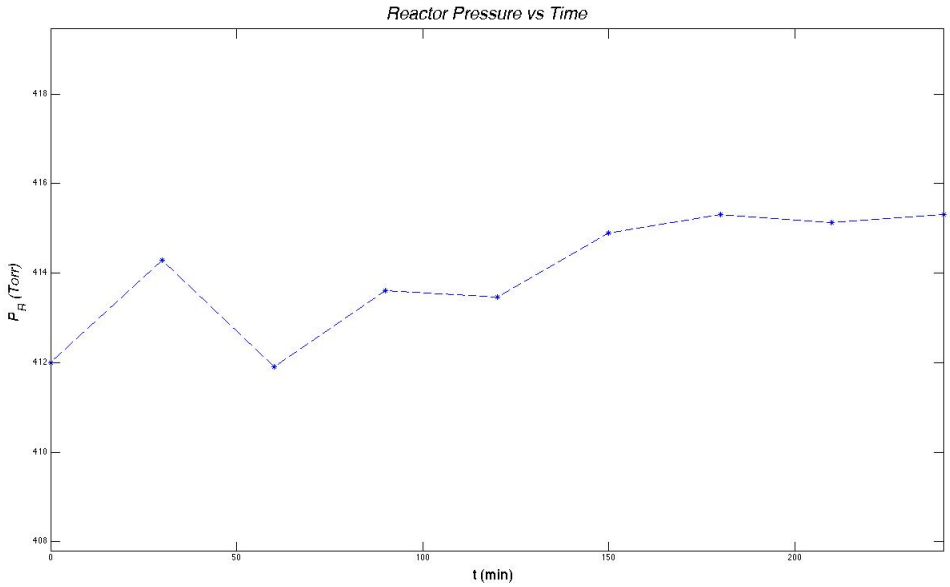

Figure 5.13 Reactor pressure-time data for experiment with ZG-.025Er sample.

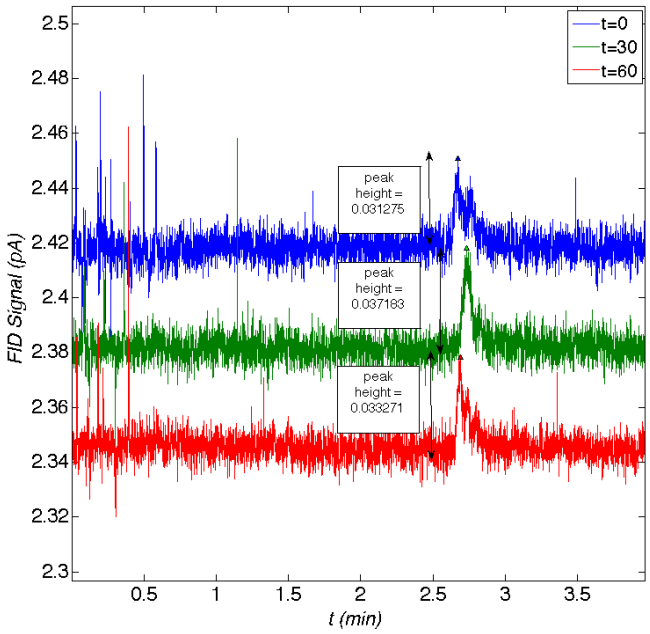

Figure 5.14 GC data for Control-3V experiment showing zero hydrocarbon peaks under visible light.

CHAPTER 6: CONCLUSIONS AND FUTURE WORK

6.1 Conclusions

The scope of the work described in this document involved designing and fabricating a photoreactor that offers improved capabilities for photocatalyst material testing, evaluating the performance of the photoreactor, and synthesizing a photocatalyst with rare earth metal ion dopants in hopes for an increased activity towards CO_2 conversion.

Chapter 3 introduced the design of a novel batch reactor system that contains a porous support that allows the recirculating reaction mixture to flow by the reacting surface of the photocatalyst. The support was included in the design to improve catalyst and light utilization, as it holds the photocatalyst directly below an LED mounted to a threaded mount fastened to the top of the reactor cell. After determining Viton® and Kalrez® o-ring materials photochemically degrade in the presence of UV light, silicone o-ring materials were found to have the highest resistance to photochemical degradation due to their inorganic makeup. Therefore, it is recommended to use silicone o-ring materials over other organic elastomer o-ring materials.

Lastly, chapter 2 discussed the synthesis and characterization of the pure and doped ZG photocatalysts as well as their respective LDH precursors. The XRD data for the LDH precursors suggested that multiple phases come about after aging the mother liquor for 22 hours at 80˚C. The two phases identified were $Zn/Ga/CO_3$ LDH and the β-Ga_2O_3 phase. Moreover, the addition of Er^{3+} into the LDH resulted in broadening of the diffraction peaks, suggesting a local deviation of d-spacings as a result of the substitution of Ga^{3+} with Er^{3+} at the M(III) site. It is also proposed

that stirring during the precipitation step yields a more crystalline product due to an increase in the Ga^{3+} and Zn^{2+} mobility to the oxygen octahedral sites resulting in the formation of a more homogeneous precipitate.

The nitridation of the pure and erbium-doped LDH precursors resulted in the formation of a solid solution of ZnO and GaN, as well as a secondary phase of Er_2O_3 in the doped samples. Consequently, it was concluded that the Er^{3+} ions did not go into the structure of the oxynitride solid solution. These findings were elucidated in the XRD and SEM data, as the XRD data showed peaks that coincide with a solid solution of ZnO and GaN as well as the cubic structure of Er_2O_3. This was supported by the SEM images revealing hexagonal plates and prisms that coincide with the solid solution along with smaller stringy structures corresponding to the Er_2O_3 phase. Additionally, the results from the N_2 physisorption experiments support the analysis of the XRD and SEM data in that an increase in specific surface area in the ZG-.025Er sample from the ZG sample indicates the presence of the less crystalline Er_2O_3 phase.

The data from the photocatalytic experiments were misleading, as any hydrocarbons detected during those experiments cannot be verified to be the result of a photocatalytic reaction due to the presence of hydrocarbons during the control-1V and control-1K experiments. Due to the absence of hydrocarbons during the control-3V experiment with a VIS LED and Viton® o-ring, it was concluded that the Viton® and Kalrez® o-rings were photochemically degrading in the presence of UV light. The control-1S experiment yielded no hydrocarbons after 90 minutes. Thus, it is recommended to use silicone o-rings to prevent misinterpretation of results if one plans to perform photocatalytic studies using a UV light source.

6.2 Future Work

6.2.1 Reactor Modifications

While the proposed photoreactor design presented in this work is an improvement from previously used systems within our research group and within the photocatalysis community, room for improvement is still apparent. The versatility could be improved by replacing the pressure sensor with one that has a greater maximum operating pressure, as it may be of interest to investigate reactions at pressures above 10,000 Torr. Moreover, the current pressure sensor is unreliable, as the average pressure reading at atmospheric conditions was 428 Torr which is 332 Torr lower than atmospheric pressure at sea level. Additionally, the addition of a filter element having a rating of 8 microns nominal at the inlet port of the compressor would protect the valve seats from foreign particulate contamination, such as catalyst powder and septum bits, and prevent any unnecessary drops in pump performance.

The current configuration of the photoreactor system leaves room for user error. The addition of electronically switched valves for CO_2 and N_2 entering the system would help minimize this potential for user error by allowing the use to open and close the valves in a more controlled fashion, resulting in more precise gas delivery. To reduce the potential for human-induced error even further, the entire photocatlaytic experimental procedure could be automated using a virtual instrument platform, such as LabVIEW, to perform each step in the procedure sequentially. Included in this automated arrangement would be an automatic rotary valve at the inlet of the GC to automatically switch the multiport valve periodically to allow a small portion of the reaction mixture to enter the GC column for a short period of time. This automatic sampling configuration would virtually eliminate the human error involved with manually injecting the sample via syringe.

6.2.2 Band Edge Measurements of ZnO/GaN

Although the values of the bandgaps for the pure and Er-doped ZG samples were calculated using DRS data and the Kubelka-Munk function, there is no way to obtain the band edge potentials using this method. Since it is the value of the band edge potentials that ultimately determine whether or not a photocatalytic reaction is thermodynamically feasible, it would be ideal to have this data to establish the suitability of the as synthesized ZG materials towards photocatalytic conversion of CO_2. This data can be obtained through the use of electrochemical impedance spectroscopy (EIS), or x-ray photoelectron spectroscopy (XPS). The result of these techniques is either the value of the maximum valence band energy (E_{VBM}) for XPS, or the minimum conduction band energy (E_{CBM}) for EIS. The resulting band edge potential, along with the calculated bandgap (E_G), can then be used to determine the value of the other band edge potential using the equation: $E_G=E_{CBM}-E_{VBM}$. If the band edge potentials of the pure and Er-doped ZG samples align correctly with the reduction and oxidation potentials for CO_2 conversion, then the photocatalytic activity of those samples should be studied in the presence of visible light.

6.2.3 Upconversion Photoluminescence of Er-Doped ZnO/GaN

Due to the limitations of the available resources in the lab, the Er-doped ZG samples were never successfully tested for upconversion luminescence. In order to do these experiments, the spectrofluorometer in our lab (ISS PC1) would need to be brought back to a fully functioning condition. Once the instrument is fixed, the samples could then be assessed for upconversion luminescence by exciting the sample with a VIS and/or IR light source and measuring the UV and/or VIS emission. If emission at an energy greater than the excitation energy is observed, it can then be concluded that the material allows the upconversion process to occur.

6.2.4 Optimizing Performance of ZnO/GaN Materials

A major limitation of semiconductors for use in photocatalysis is the recombination of photoexcited electrons and holes. Therefore, one way of evaluating the performance of a photocatalyst is to measure the rate of recombination. This can be done using techniques such as ultrafast spectroscopy, and photoluminescence. A great deal of work is involved in tuning a semiconductor to yield the lowest recombination rate. Several methods have been investigated and have proven to yield favorable results. Some of these methods include: doping with precious metals to "trap" excited electrons at the surface, and decreasing the length of the carrier diffusion path. Future work in our research group may involve applying some of these techniques. For example, synthesizing ultra thin ZG structures such as nanotubes, nanoplates, or nanoflowers can shorten the carrier diffusion path. The optimal performance from the ZG samples may be possible using a combination of both techniques to minimize recombination.

REFERENCES

[1] J. H. Scofield, “Chapter 3 : the Solar Spectrum the Stefan-Boltzmann Law the Planck Distribution,” pp. 1–9, 2009.

[2] Florida Department of Environmental Protection, “62-296.405 Fossil Fuel Steam Generators with More than 250 Million Btu Per Hour Heat Input,” in *Florida Administrative Code*, 2014.

[3] Center for Climate and Energy Solutions, “Q & A : EPA Regulation of Greenhouse Gas Emissions from Existing Power Plants,” no. February, pp. 1–8, 2014.

[4] N. Guettaï and H. Ait Amar, “Photocatalytic oxidation of methyl orange in presence of titanium dioxide in aqueous suspension. Part I: Parametric study,” *Desalination*, vol. 185, no. 1–3, pp. 427–437, 2005.

[5] S. N. Habisreutinger, L. Schmidt-Mende, and J. K. Stolarczyk, “Photocatalytic reduction of CO2 on TiO2 and other semiconductors.,” *Angew. Chem. Int. Ed. Engl.*, vol. 52, no. 29, pp. 7372–408, Jul. 2013.

[6] M. Tahir and N. S. Amin, “Photocatalytic CO2 reduction and kinetic study over In/TiO2 nanoparticles supported microchannel monolith photoreactor,” *Appl. Catal. A Gen.*, vol. 467, pp. 483–496, Oct. 2013.

[7] W. Qin, D. Zhang, D. Zhao, L. Wang, and K. Zheng, “Near-infrared photocatalysis based on YF3 : Yb3+,Tm3+/TiO2 core/shell nanoparticles.,” *Chem. Commun. (Camb).*, vol. 46, no. 13, pp. 2304–6, Apr. 2010.

[8] O. Ola and M. M. Maroto-Valer, “Review of material design and reactor engineering on TiO2 photocatalysis for CO2 reduction,” *J. Photochem. Photobiol. C Photochem. Rev.*, vol. 24, pp. 16–42, Sep. 2015.

[9] J. Wang, B. Huang, Z. Wang, P. Wang, H. Cheng, Z. Zheng, X. Qin, X. Zhang, Y. Dai, and M.-H. Whangbo, “Facile synthesis of Zn-rich (GaN)1−x(ZnO)x solid solutions using layered double hydroxides as precursors,” *J. Mater. Chem.*, vol. 21, no. 12, p. 4562, 2011.

[10] J. He, M. Wei, B. Li, Y. Kang, D. G. Evans, and X. Duan, “Preparation of Layered Double Hydroxides,” in *Layered Double Hydroxides*, 1st ed., vol. 119, no. September 2005, X. Duan and D. G. Evans, Eds. Springer Berlin Heidelberg, 2006, pp. 89–119.

[11] A. de Roy, C. Forano, and J. P. Besse, *Layered Double Hydroxides: Present and Future*. Nova Science Publishers, Inc., 2006.

[12] Y. Lee, S. Hu, W. Water, and Y. Huang, “Improved optical and structural properties of ZnO thin films by rapid thermal annealing,” *Solid state …*, vol. 143, no. 4–5, pp. 250–254, Jul. 2007.

[13] U. Schühle and J.-F. Hochedez, “Solar-blind UV detectors based on wide band gap semiconductors,” in *Observing Photons in Space*, vol. 9, M. C. E. Huber, A. Pauluhn, J. L. Culhane, J. G. Timothy, K. Wilhelm, and A. Zehnder, Eds. New York City: Springer New York, 2013, pp. 467–477.

[14] B. Adeli and F. Taghipour, “A Review of Synthesis Techniques for Gallium-Zinc Oxynitride Solar-Activated Photocatalyst for Water Splitting,” *ECS J. Solid State Sci. Technol.*, vol. 2, no. 7, pp. Q118–Q126, Jun. 2013.

[15] K. Maeda and K. Domen, “New Non-Oxide Photocatalysts Designed for Overall Water Splitting under Visible Light,” *J. Phys. Chem. C*, vol. 111, no. 22, pp. 7851–7861, Jun. 2007.

[16] T. Hisatomi, K. Maeda, D. Lu, and K. Domen, “The effects of starting materials in the synthesis of (Ga(1-x)Znx)(N(1-x)O(x)) solid solution on its photocatalytic activity for overall water splitting under visible light.,” *ChemSusChem*, vol. 2, no. 4, pp. 336–43, Jan. 2009.

[17] K. Maeda, T. Takata, M. Hara, N. Saito, Y. Inoue, H. Kobayashi, and K. Domen, “GaN:ZnO solid solution as a photocatalyst for visible-light-driven overall water splitting.,” *J. Am. Chem. Soc.*, vol. 127, no. 23, pp. 8286–7, Jun. 2005.

[18] M. M. Debusk, A. C. Buchanan, and C. K. Narula, “PHOTOCATALYTIC CONVERSION OF CO 2 – AN ALTERNATE TO STORAGE BASED SEQUESTRATION,” in *ACS National Meeting*, 2009, no. March.

[19] S. Yu, C. Chen, and J. C. S. Wu, “Visible light photocatalytic reduction of Carbon Dioxide to produce renewable resources,” in *The 6th Asia-Pacific Congress on Catalysis*, 2013.

[20] P. Zhou, H. L. Gao, S. C. Yan, and Z. G. Zou, “The Kirkendall effect towards oxynitride nanotubes with improved visible light driven conversion of CO 2 into CH 4,” *Dalt. Trans.*, vol. 45, no. 8, pp. 3480–3485, Feb. 2016.

[21] Y. T. Liang, B. K. Vijayan, K. A. Gray, and M. C. Hersam, “Minimizing graphene defects enhances titania nanocomposite-based photocatalytic reduction of CO2 for improved solar fuel production,” *Nano Lett.*, vol. 11, no. 7, pp. 2865–2870, 2011.

[22] M. Anpo, H. Yamashita, Y. Ichihashi, and S. Ehara, “Photocatalytic reduction of CO2 with H2O on various titanium oxide catalysts,” *J. Electroanal. Chem.*, vol. 396, no. 1–2, pp. 21–26, Oct. 1995.

[23] R. Adhikari, G. Gyawali, S. H. Cho, R. Narro-García, T. Sekino, and S. W. Lee, “Er3+/Yb3+co-doped bismuth molybdate nanosheets upconversion photocatalyst with enhanced photocatalytic activity,” *J. Solid State Chem.*, vol. 209, pp. 74–81, Jan. 2014.

[24] D. Phifer, L. Tuma, T. Vystavel, P. Wandrol, and R. J. Young, “Improving SEM Imaging Performance Using Beam Deceleration,” *Micros. Today*, vol. 17, no. 04, p. 40, Jun. 2009.

[25] H. S. Fogler, *Elements of Chemical Reaction Engineering*, 4th ed. Westford: Prentice Hall Professional Technical Reference, 2006.

[26] Parker Hannifin Corporation Technical Staff, *Parker O-Ring Handbook*. Lexington: Parker Hannifin Corporation, 2007.

[27] Matheson Tri-Gas Technical Staff, *INSTRUCTION MANUAL PURGING HIGH PURITY GAS DELIVERY SYSTEMS*. Montgomeryville: Matheson Tri-Gas.

[28] Senior Aerospace Metal Bellows Technical Staff, *MB-21/41 Standard Operating Instructions*. Sharon: Senior Aerospace Metal Bellows.

[29] G. S. Thomas and P. V. Kamath, “The layered double hydroxide (LDH) of Zn with Ga: Synthesis and reversible thermal behaviour,” *Solid State Sci.*, vol. 8, no. 10, pp. 1181–1186, 2006.

[30] S. Speakman, “Estimating crystallite size using xrd.” MIT Center for Materials Science and Engineering, Cambridge, pp. 1–105, 2011.

[31] L. Li, W. Wei, and M. Behrens, “Synthesis and characterization of a-, b-, and g-Ga2O3 prepared from aqueous solutions by controlled precipitation,” *Solid State Sci.*, vol. 14, no. 7, pp. 971–981, 2012.

[32] S. Shet, Y. Yan, H. Wang, N. Ravindra, J. Turner, and M. Al-Jassim, “ZnO:GaN thin films for photoelectrochemical water splitting application,” *Emerg. Mater. Res.*, vol. 1, no. 4, pp. 201–204, Aug. 2012.

[33] N. Guskos, J. Majszczyk, J. Typek, G. Zolnierkiewicz, E. Tomaszewicz, and K. Aidinis, “Relative intensities of f-f transitions of erbium(III) ion studied by photoacoustic spectroscopy,” *Rev. Adv. Mater. Sci.*, vol. 23, no. 1, pp. 97–101, 2010.

[34] G. Feng, S. Liu, Z. Xiu, Y. Zhang, J. Yu, Y. Chen, P. Wang, and X. Yu, “Visible Light Photocatalytic Activities of TiO 2 Nanocrystals Doped with Upconversion Luminescence Agent,” *J. Phys. Chem. C*, vol. 112, no. 35, pp. 13692–13699, Sep. 2008.

[35] Y. Yang, C. Zhang, Y. Xu, H. Wang, X. Li, and C. Wang, “Electrospun Er:TiO2 nanofibrous films as efficient photocatalysts under solar simulated light,” *Mater. Lett.*, vol. 64, no. 2, pp. 147–150, 2010.

[36] P. J. Statham, “Limitations to accuracy in extracting characteristic line intensities from x-ray spectra,” *J. Res. Natl. Inst. Stand. Technol.*, vol. 107, no. 6, p. 531, 2002.

APPENDICES

Appendix A: MATLAB Programs

A.1 Bandgap GUI

```
function Bandgap_GUI
    clear all
    clc

    f=figure('visible','off',...
        'Position',[360,500,450,285]);

    hb=uicontrol('Style','pushbutton',...
        'String','Browse',...
        'Position',[315,190,90,20],...
        'Callback',@drs_Callback);
    hb2=uicontrol('Style','pushbutton',...
        'String','Calculate',...
        'Position',[315,80,90,20],...
        'Callback',@kmf_Callback);
    hb3=uicontrol('Style','pushbutton',...
        'String','Clear',...
        'Position',[315,50,90,20],...
        'Callback',@clear_Callback);
    htext=uicontrol('Style','text',...
        'String','Upload DRS data',...
        'Position',[315,220,90,20]);
    string=['Direct allowed transition, n = 1/2|',...
        'Direct forbidden transition,n = 3/2|',...
        'Indirect allowed transition, n = 2|',...
        'Indirect forbidden transition, n = 3'];
    htext2=uicontrol('Style','text',...
        'String','BG = ',...
        'Position',[315,20,90,20]);
    hpopup=uicontrol('Style','popup',...
        'String',string,...
        'Position',[300,115,120,25],...
        'Callback',{@popup_menu_Callback});
    htext3=uicontrol('Style','text',...
        'String','Select mode of electronic transition',...
        'Position',[305,150,110,30]);
    ha = axes('Units','Pixels','Position',[50,60,200,185]);
    hxlab=xlabel('\ith\nu(eV)');
    hylab=ylabel('\it(h\nuF(R_\infty))^1^/^n',...
                    'VerticalAlignment','baseline');
    htit=title('\itTauc Plot');

    % Initialize the GUI.
    % Change units to normalized so components resize
    % automatically.
    set([f,ha,hxlab,hylab,htit,hb,hb2,hb3,htext,htext3,htext2,hpopup],...
        'Units','normalized');
    align([hb,hb2,hb3,htext,htext2,htext3,hpopup],'Center','None');
    % Assign the GUI a name to appear in the window title.
    set(f,'Name','Bandgap GUI')
    % Move the GUI to the center of the screen.
    movegui(f,'center')
    % Make the GUI visible.
```

```
set(f,'Visible','on');
hold all
DRS=0;
n=0;


function popup_menu_Callback(hObj,event) %#ok<INUSD>
    % Called when user activates popup menu
    val = get(hObj,'Value');
        if val==1
            n=.5;
            hylab=ylabel('\it(h\nuF(R_\infty))^2',...
                'VerticalAlignment','baseline');
        elseif val==2
            n=1.5;
            hylab=ylabel('\it(h\nuF(R_\infty))^2^/^3',...
                'VerticalAlignment','baseline');
        elseif val==3
            n=2;
            hylab=ylabel('\it(h\nuF(R_\infty))^1^/^2',...
                'VerticalAlignment','baseline');
        elseif val==4
            n=3;
            hylab=ylabel('\it(h\nuF(R_\infty))^1^/^3',...
                'VerticalAlignment','baseline');
        end
        set(hylab,'Units','normalized');
end

function drs_Callback(hObj,event)
    DRS=uiimport('-file');
    DRS=struct2cell(DRS);
    DRS=cell2mat(DRS);
end

function kmf_Callback(hObj,event)
    h=6.626e-34;    % Planck's constant (m^2*kg/s)
    c=3e8;  % speed of light (m/s)
    %% KUBELKA MUNK

    % The Kubleka Munk function
    kmf=zeros(length(DRS),2);

    for i=1:length(DRS)
        kmf(i,1)=(h*c/(DRS(i,1)*10^(-9)))/1.6022e-19;
        kmf(i,2)=(h*(c/(DRS(i,1)/10^9))*(1-DRS(i,2)/100)^2/...
            (2*DRS(i,2)/100)/(1.6022e-19))^(1/n);
    end

    % First derivative of Kubleka Munk function
    % calculated using forward difference method.
    dkmf=zeros(length(DRS)-1,2);
    for i=1:length(dkmf)
        dkmf(i,1)=kmf(i,1);
        dkmf(i,2)=(kmf(i+1,2)-kmf(i,2))/(kmf(i+1,1)-kmf(i,1));
    end
```

```
        for i=1:20
            dkmf(:,2)=smooth(dkmf(:,2));    % Smooth the derivative
        end

        %% BANDGAP

        % The bandgap is defined as the x-intercept of the line tangent to
        % the point of inflection of the Kubelka Munk function. The point
        % of inflection is located by finding the local maximum slope of
        % the Kubelka Munk function.

        % LOCAL MAXIMUM OF DERIVATIVE OF KUBELKA MUNK FUNCTION.

        [pks,locs]=findpeaks(dkmf(:,2));
        for i=1:length(locs)
            for j=i:length(locs)
                check1=locs(j)-locs(i);
                check2=pks(j)-pks(i);
                if check1>80 & check2>0
                    m(1)=pks(i);
                    m(2)=pks(j);
                elseif check2<0
                    m=zeros(length(locs),1);
                    m(1)=max(pks);
                end
            end
        end

        % Define a function for the line tangent to the point of inflection
        % by using the point-slope equation [i.e. y-y1=m*(x-x1)].
        y1=kmf(find(dkmf==m(1)));
        x1=kmf(find(dkmf==m(1))-length(kmf));
        y=@(x)m(1)*(x-x1)+y1;
        BG=fsolve(y,2.5);
        lambda=h*c/(BG*1.6022e-19*10^-9);
        string2=sprintf('BG = %.2f eV',BG);
        set(htext2,'String',string2)

        %% PLOTS

        % Tauc Plot
        plot(kmf(:,1),kmf(:,2),'k')

        axis([kmf(1,1) max(kmf(:,1)) 0 1.1*(max(kmf(:,2)))])
        fplot(y,[kmf(1,1) (1.1*(kmf(find(kmf==max(kmf(:,2)))...
            -length(kmf))-kmf(1))+kmf(1)) 0 (max(kmf(:,2))+1)],'r')

    end

    function clear_Callback(hObj,event)
        cla
        set(htext2,'String','BG = ')
    end
end
```

A.2 XRD Analysis Program

```
clc
clear all

d=uigetdir;
cd(d)
fileID=fopen('output.txt','w');
time=clock;
if time(5)==0
    if time(4)>=12 & time(4)<13
        string='Program executed at %.0f:00 P.M. on %s\n\n';
        fprintf(fileID,string,time(4),date);
    elseif time(4)>=13 & time(4)<24
        string='Program executed at %.0f:00 P.M. on %s\n\n';
        fprintf(fileID,string,time(4)-12,date);
    elseif time(4)<12
        string='Program executed at %.0f:00 A.M. on %s\n\n';
        fprintf(fileID,string,time(4),date);
    elseif time(4)>=24
        string='Program executed at %.0f:00 A.M. on %s\n\n';
        fprintf(fileID,string,time(4)-12,date);
    end
elseif time(5)>0 & time(5)<=9
    if time(4)>=12 & time(4)<13
        string='Program executed at %.0f:0%.0f P.M. on %s\n\n';
        fprintf(fileID,string,time(4),time(5),date);
    elseif time(4)>=13 & time(4)<24
        string='Program executed at %.0f:0%.0f P.M. on %s\n\n';
        fprintf(fileID,string,time(4)-12,time(5),date);
    elseif time(4)<12
        string='Program executed at %.0f:0%.0f A.M. on %s\n\n';
        fprintf(fileID,string,time(4),time(5),date);
    elseif time(4)>=24
        string='Program executed at %.0f:0%.0f A.M. on %s\n\n';
        fprintf(fileID,string,time(4)-12,time(5),date);
    end
else
    if time(4)>=12 & time(4)<13
        string='Program executed at %.0f:%.0f P.M. on %s\n\n';
        fprintf(fileID,string,time(4),time(5),date);
    elseif time(4)>=13 & time(4)<24
        string='Program executed at %.0f:%.0f P.M. on %s\n\n';
        fprintf(fileID,string,time(4)-12,time(5),date);
    elseif time(4)<12
        string='Program executed at %.0f:%.0f A.M. on %s\n\n';
        fprintf(fileID,string,time(4),time(5),date);
    elseif time(4)>=24
        string='Program executed at %.0f:%.0f A.M. on %s\n\n';
        fprintf(fileID,string,time(4)-12,time(5),date);
    end
end

%% IMPORT DATA
xydata=uiimport('-file');
xydata=struct2cell(xydata);
xydata=cell2mat(xydata);
```

```
fprintf(fileID,'Imported xydata\n');

xdata=xydata(:,1);
ydata=xydata(:,2);
ydata=smooth(ydata);

%% SET THE PLOT PROPERTIES
cl='y';
if cl=='y'|'Y'
    close
elseif cl=='n'|'N'
    figure
elseif isempty(cl)
    close
end

AxFntsz=22;
plot(xdata,ydata)
axis([xdata(1) xdata(length(xdata)) 0 (1.05*max(ydata))])
set(gca,'fontsize',AxFntsz)
set(gcf,'outerposition',[1 5 874 874])
set(gca,'plotboxaspectratio',[1 1 1])
xlabel('\it2\theta','fontsize',22)
ylabel('\itCounts','fontsize',22)

%%
disp('Select data for baseline values using the brush tool in the figure
window.')
disp('Create a variable from the selected data and name the variable "bld".')

%%
hold on
linkdata on
shg

%% Search for peaks in 1st sample
string=['\n\nSpecify the order you would like to return the peak list:',...
    '\n\nType 1 to return peaks in increasing order from smallest to',...
    ' largest value.',...
    '\nType 2 to return peaks in decreasing order from largest to',...
    ' smallest value.',...
    '\nType 3 to return peaks in the order they occur in the input',...
    ' data.\n\n'];
resp=input(string);
steps=zeros(length(xdata)-1,1);

for i=1:length(steps)
    steps(i)=xdata(i+1,1)-xdata(i,1);
end

msteps=mean(steps);
mnpkd1=ceil(.62/msteps);
m=mean(bld(:,1));
mnpkht=2.75*m;
thr=.15;
```

```
if resp==1
    arrng='ascend';
elseif resp==2
    arrng='descend';
elseif resp==3
    arrng='none';
elseif isempty(resp)
    arrng='none';
end

[pks,locs]=findpeaks(ydata(:,1),'minpeakheight',mnpkht,...
    'minpeakdistance',mnpkd1,...
    'threshold',thr,...
    'sortstr',arrng);

%% Plot peaks
plot(xdata(locs),ydata(locs),'k^','markerfacecolor','b');
shg

%% Calculate Crystallite Size Using Scherrer Equation
lambda=1.54e-10; % Radiation source wavelength [nm]
K=0.9;  % Proportionality constant for hexagonal structures
k=1;
n=1;
a=1.2;
b=30;
fprintf(fileID,'Begin outermost while loop:\n');

while n
    fprintf(fileID,'\titeration %.0f of outermost while loop\n',k);
    fprintf(fileID,'\tAlocate memory for vectors created in for loop\n');
    % Alocate memory for vectors created in for loop
    hm=zeros(length(pks),1);    % Half of peak height relative to baseline
    lhmy=zeros(length(pks),1);  % Y-values on left side of peak at half max
    lhmx=zeros(length(pks),1);  % X-values on left side of peak at half max
    rhmy=zeros(length(pks),1);  % Y-values on right side of peak at half max
    rhmx=zeros(length(pks),1);  % X-values on right side of peak at half max
    fwhm=zeros(length(pks),1);  % Width of peak at half max [degrees]
    angle=zeros(length(pks),1); % Angle values of peak centers [degrees]
    tau=zeros(length(pks),1);   % Crystallite sizes of corresponding peaks
    L=length(pks);

    % Create for loop to identify values of x & y at half max by scanning
    % left and right sides of peak until the y-value is < half max
    fprintf(fileID,'\tBegin for loop:\n');
    for i=1:length(pks)
        fprintf(fileID,'\t\titeration %.0f of for loop\n',i);
        hm(i)=.5*(pks(i)-m)+m;
        fprintf(fileID,'\t\tcalculete angle(%.0f)\n',i);
        angle(i)=deg2rad(xdata(locs(i)));

        % scan left side of peak for x & y value at half max
        fprintf(fileID,'\t\tinitialize lhmy(%.0f)=peak val\n',i);
        lhmy(i)=ydata(locs(i)); % Initialize lhmy to be equal to peak value
        j=1;    % Initialize j for while loop
        fprintf(fileID,'\t\tbegin first while loop:\n');
        while lhmy(i)>a*hm(i)
```

```
    % eliminate peaks whos y values on left side never go lower
    % than half max.
    str=['\t\t\tchecking for high elev %.0f elements left',...
        ' of peak @ x=%.2f deg\n'];
    fprintf(fileID,str,j,xdata(locs(i)));
    if locs(i)-j==0
        string=['\t\t\t\tLeft side of peak at x=%.2f deg never',...
            ' reaches value less than hm(%.0f)\n'];
        fprintf(fileID,string,xdata(locs(i)),i);
        string='\t\t\t\tpeak deleted at x=%.2f deg.\n';
        fprintf(fileID,string,xdata(locs(i)));
        pks(i)=[];
        locs(i)=[];
        fprintf(fileID,'\t\t\t\tbreak in 1st while loop\n');
        % exit the while loop
        break
    end
    fprintf(fileID,'\t\t\televation check passed\n');
    fprintf(fileID,'\t\t\tevaluate the peak prominance\n');
    if j>=1 & j<=b & ydata(locs(i)-j)>pks(i)
        string=['\t\t\t\tPeak prominance is low.\nPeak deleted',...
            ' at x=%.2f deg.\n'];
        fprintf(fileID,string,xdata(locs(i)));
        pks(i)=[];
        locs(i)=[];
        break
    end
    fprintf(fileID,'\t\t\tdefine lhmy(%.0f)\n',i);
    lhmy(i)=ydata(locs(i)-j);
    fprintf(fileID,'\t\t\tdefine lhmx(%.0f)\n',i);
    lhmx(i)=xdata(locs(i)-j);
    % update j only if conditional statement for while loop is true
    if lhmy(i)>hm(i)
        fprintf(fileID,'\t\t\tupdate j\n');
        j=j+1;
    end
end
fprintf(fileID,'\t\tfirst while loop done\n');
fprintf(fileID,'\t\tcheck to break before second while loop\n');
string=['\t\tchecking if length(pks) is less than original',...
    ' length(pks)\n'];
fprintf(fileID,string);
if length(pks)==L
    string=['\t\t\tlength(pks)==original length(pks). continue',...
        ' in for loop\n'];
    fprintf(fileID,string);
elseif length(pks)~=L
    string=['\t\t\tlength(pks)~=original length(pks). exit for',...
        ' loop and reset L\n'];
    fprintf(fileID,string);
    break
end
% scan right side of peak for x & y value at half max
fprintf(fileID,'\t\tinitialize rhmy(%.0f)=peak val\n',i);
rhmy(i)=ydata(locs(i)); % Initialize rhmy to be equal to peak value
j=1;    % Initialize j for while loop
fprintf(fileID,'\t\tbegin second while loop:\n');
while rhmy(i)>a*hm(i)
```

```
        % eliminate peaks whos y values on right side never go lower
        % than half max.
        str=['\t\t\tchecking for high elev %.0f elements right of',...
            ' peak @ x=%.2f deg\n'];
        fprintf(fileID,str,j,xdata(locs(i)));
        if locs(i)+j>=length(ydata)
            string=['\t\t\t\tRight side of peak at x=%.2f deg',...
                ' never reaches value less than hm(%.0f)\n'];
            fprintf(fileID,string,xdata(locs(i)),i);
            pks(i)=[];
            locs(i)=[];
            fprintf(fileID,'\t\t\t\tbreak in 2nd while loop\n');
            break
        end
        fprintf(fileID,'\t\t\televation check passed\n');
        fprintf(fileID,'\t\t\tevaluate the peak prominance\n');
        if j>=1 & j<=b & ydata(locs(i)+j)>pks(i)
            string=['\t\t\t\tPeak prominance is low.\nPeak deleted',...
                ' at x=%.2f deg.\n'];
            fprintf(fileID,string,xdata(locs(i)));
            pks(i)=[];
            locs(i)=[];
            break
        end
        fprintf(fileID,'\t\t\tdefine rhmy(%.0f)\n',i);
        rhmy(i)=ydata(locs(i)+j);
        fprintf(fileID,'\t\t\tdefine rhmx(%.0f)\n',i);
        rhmx(i)=xdata(locs(i)+j);
        if rhmy(i)>hm(i)
            fprintf(fileID,'\t\t\tupdate j\n');
            j=j+1;
        end
    end
    fprintf(fileID,'\t\tsecond while loop done\n');
    string=['\t\tcheck to break before fwhm(%.0f) and tau(%.0f)',...
        ' are defined\n'];
    fprintf(fileID,string,i,i);
    string='\t\tchecking if length(pks)==original length(pks)\n';
    fprintf(fileID,string);
    if length(pks)==L
        string=['\t\t\tlength(pks)==original length(pks). continue',...
            ' in for loop\n'];
        fprintf(fileID,string);
    elseif length(pks)~=L
        string=['\t\t\tlength(pks)~=original length(pks). exit for',...
            ' loop and reset L\n'];
        fprintf(fileID,string);
        break
    end
    fprintf(fileID,'\t\tcalculate fwhm(%.0f)\n',i);
    fwhm(i)=deg2rad(rhmx(i)-lhmx(i));
    fprintf(fileID,'\t\tcalculate tau(%.0f)\n',i);
    tau(i)=(K*lambda/(fwhm(i)*cos(angle(i))))*10^9;
end
fprintf(fileID,'\tExited for loop\n\n');
if length(pks)==L
    fprintf(fileID,'\tlength(pks)==L, no peaks deleted.\n');
    n=0;
```

```
    elseif length(pks)~=L
        k=k+1;
        n=1;
    end
end
fprintf(fileID,'Outermost while loop done.\n');
tau_expected=sum((pks/sum(pks)).*tau);
mtau=mean(tau);
str=['\nThe average value of the crystallite size is:',...
    '\n\n\tD_avg = %.3f nm\n\n'];
fprintf(fileID,str,mtau);
fprintf(str,mtau);
str=['The expected value of the crystallite size is:',...
    '\n\n\tD_exp = %.3f nm\n\n'];
fprintf(fileID,str,tau_expected);
fprintf(str,tau_expected);
str=['Crystallite size of largest peak at x=%.2f deg:\n\n\tD_pmax',...
    ' = %.3f nm\n'];
fprintf(fileID,str,xdata(locs(find(pks==max(pks)))),...
    tau(find(pks==max(pks))));
fprintf(str,xdata(locs(find(pks==max(pks)))),tau(find(pks==max(pks))));
fclose(fileID);

hold off
linkdata off
plot(xdata,ydata)
axis([xdata(1) xdata(length(xdata)) 0 (1.05*max(ydata))])
set(gca,'fontsize',AxFntsz)
set(gcf,'outerposition',[1 5 874 874])
set(gca,'plotboxaspectratio',[1 1 1])
xlabel('\it2\theta','fontsize',22)
ylabel('\itCounts','fontsize',22)
hold on
plot(xdata(locs),ydata(locs),'k^','markerfacecolor','b');
shg
```

Appendix B: Instrumentation

B.1 Gas Chromatograph

To analyze the gaseous samples taken from the photoreactor during the photocatalytic and control experiments the samples were injected via syringe into the split/splitless inlet of the Agilent Technologies 7890A GC System. A photograph of the GC is given in Figure B.1 below.

Figure B.1 Agilent Technologies 7890A GC System.

B.1.1 Column

The column used in this study is an Agilent GS-CarbonPLOT capillary column with a length of 30 m and an inner diameter of 0.32 mm. The stationary phase is a hydrophobic carbon molecular sieve that allows the user to inject samples containing water without noticing any peak retention time shifts. This was an important factor in choosing a column, as the samples taken from the reactor contain water in the form of saturated vapor. An image of the capillary column installed in the GC is given in Figure B.2 below.

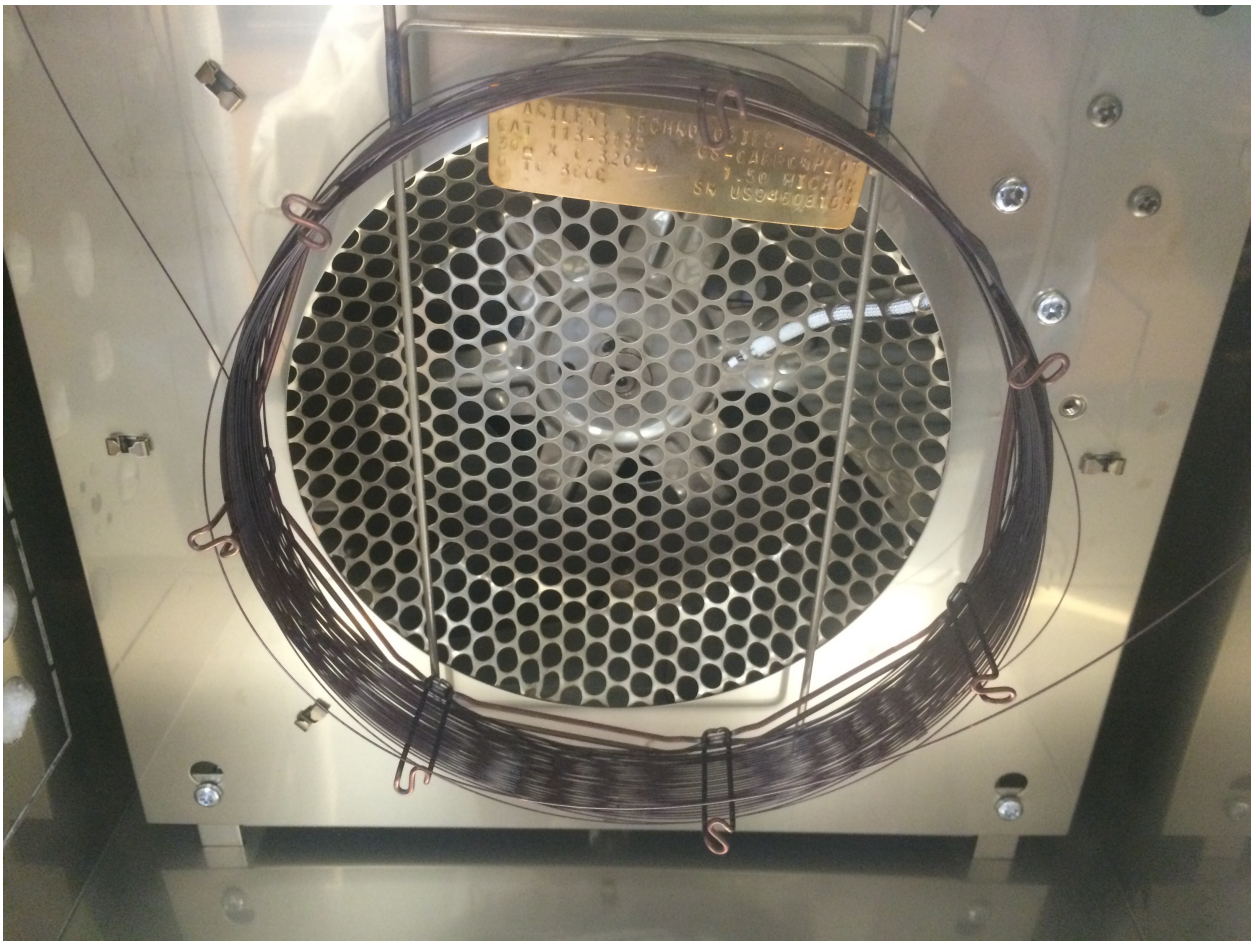

Figure B.2 Agilent Technologies GS-CarbonPLOT capillary column installed in the GC oven.

B.1.2 Detector

The detector used in this study is a flame ionization detector (FID). An FID uses an air-hydrogen flame to burn effluent from the column outlet and two electrodes as the detector that polarize the flame and collect any ions formed during combustion. The FID is limited to hydrocarbon samples only, as components containing carbon yield the highest response. An image of the FID is provided in Figure B.3 below.

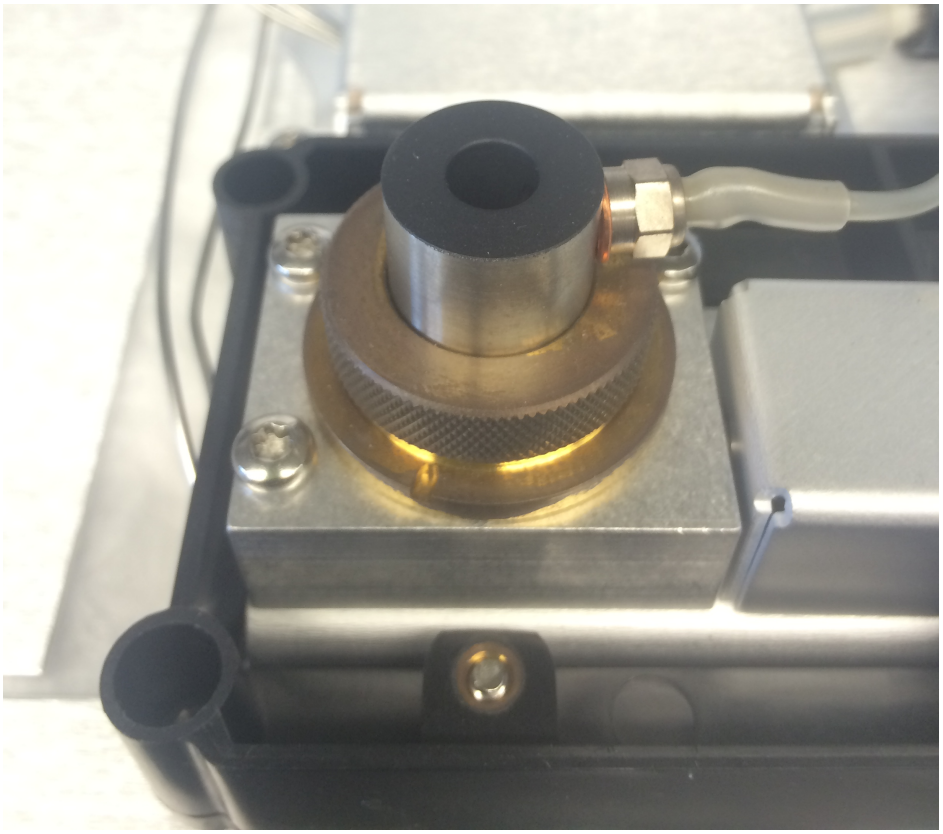

Figure B.3 FID

Figure B.4 Bruker D8 ADVANCE diffractometer with a Cu Kα (λ = 0.154 nm) radiation source.

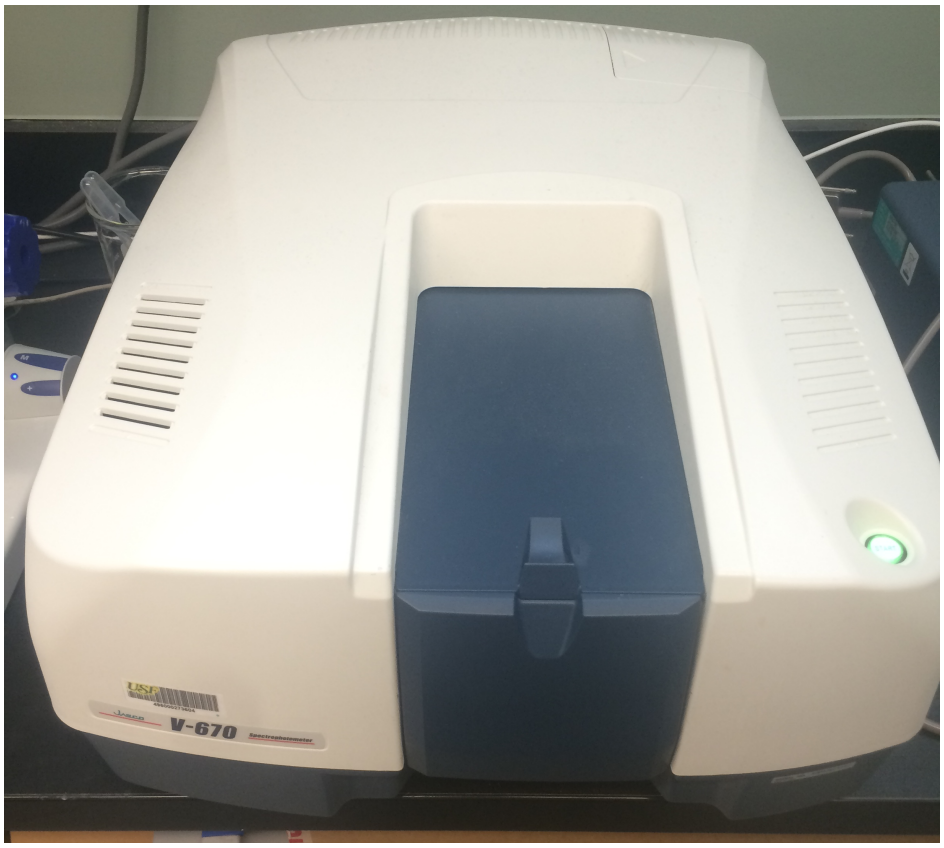

Figure B.5 Jasco V-670 UV/VIS Spectrophotometer with a Jasco ISN-723 integrating sphere

Appendix C: Supplementary Data

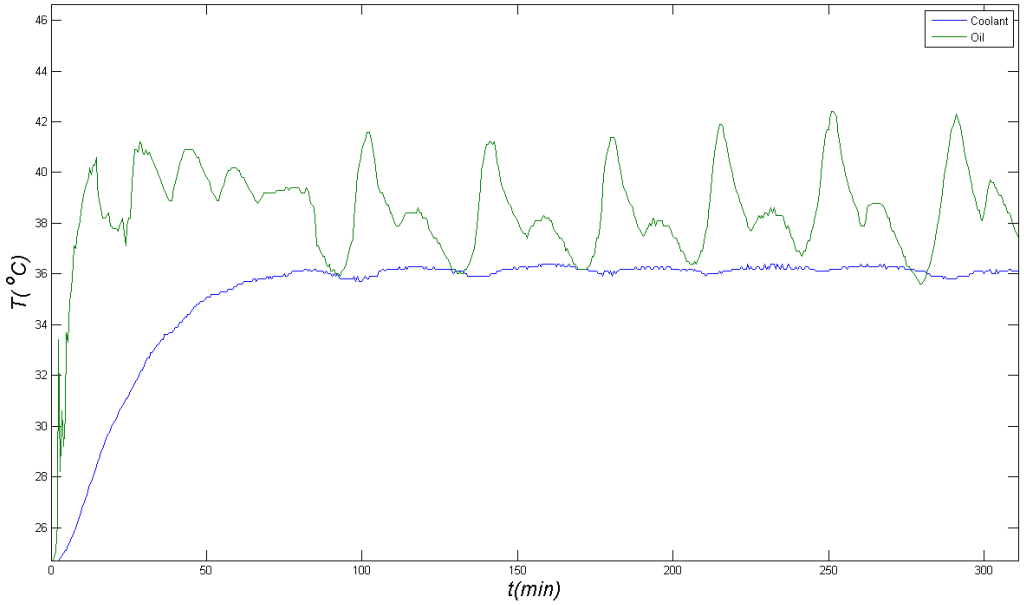

Figure C.1 Steady state temperature of oil bath and bubbler.

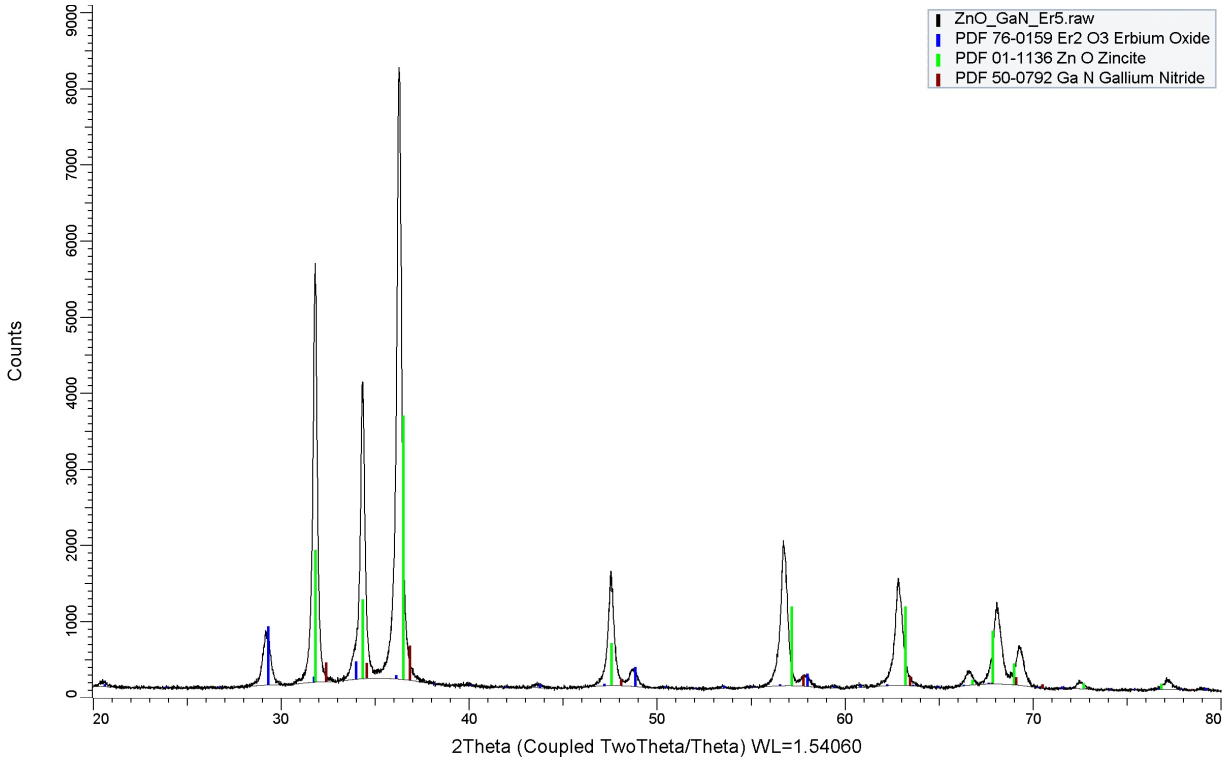

Figure C.2 XRD peak search results for ZG-.05Er sample (ICDD PDF-2 2004).

Table C.1 Specifications for Thorlabs M405L2 LED.

Specification	Value
Nominal Wavelength	405 nm
Power LED Output (Min)	410 mW
Power LED Output (Typical)	760 mW
Test Current for Typical LED Power	1000 mA
Maximum Current (CW)	1000 mA
Forward Voltage	3.8 V
Bandwidth (FWHM)	13 nm
Viewing Angle	85˚
Typical Lifetime	100,000 h

Table C.2 Actual reaction parameters for photocatalytic and control experiments.

Exp. #	Catalyst	T_B (°C)	T_R* (°C)	m_{cat} (g)	LED_P (%)	P_{R1}** (Torr)	P_{R2}*** (Torr)	λ (nm)	t_{RXN} (h)	t_{SPL} (h)
1	-	32.1	48.6	0	100	414.30	415.10	405	4	0.5
2	P25	31.6	40.8	0.0202	0	437.00	448.00	405	4	0.5
3	P25	31.3	50.2	0.0202	100	427.00	428.30	405	4	0.5
4	ZG	31.6	51.5	0.0205	100	410.28	420.00	405	4	0.5
5	ZG-.025Er	31.7	53.1	0.0204	100	414.00	420.00	405	4	0.5
6	ZG-.05Er	31.5	52.3	0.0200	100	424.04	425.70	405	4	0.5
7	ZG-.10Er	31.9	53.7	0.0206	100	419.00	425.30	405	4	0.5

* Values for T_R are average temperature over total experiment time

** Values for P_{R1}, taken immediately after N_2 purge, are absolute pressure and assumed to be equivalent to atmospheric pressure. Recorded values are below atmospheric due to a faulty sensor.

*** Values for P_{R2} were taken immediately after charging CO_2 and are absolute pressure. Recorded values are below atmospheric due to a faulty sensor.